Journal of Materials Chemistry A

ROYAL SOCIETY OF CHEMISTRY

REVIEW

View Article Online
View Journal

Cite this: DOI: 10.1039/d6ta01432a

High-entropy alloy electrocatalysts for oxygen reduction and hydrogen evolution reactions: recent advances and future perspectives

Peichen Wang,†[a] Shiqi Wang,†[b] Łukasz Kurpaska,[a] Haixian Yan,[b] Silvia Bonfanti,[a] Bo Weng, *[cd] Pedro H. C. Camargo *[b] and Wenyi Huo *[a]

The growing demand for sustainable energy conversion underscores the need for efficient electrocatalysts for the oxygen reduction reaction (ORR) in fuel cells and metal–air batteries, and for the hydrogen evolution reaction (HER) in water electrolysis. High-entropy alloys (HEAs), enabled by multi-principal-element design and high-entropy core effects, offer a promising alternative to costly noble-metal catalysts by combining tunable electronic structures, multi-site/ensemble effects, and potentially improved durability. This review summarizes recent progress in HEA electrocatalysts for the ORR and HER. We discuss reaction mechanisms and key activity/stability metrics in acidic and alkaline media and provide bibliometric insights highlighting the rapid growth of the field and the prevalence of 3d-transition-metal-rich compositions. Reported catalyst performances are further organized by composition dominance (3d/4d/5d transition metals) and linked to electronic-structure considerations, alongside an overview of representative synthetic strategies. Finally, we outline the remaining challenges and provide an outlook toward practical electrochemical applications.

Received 15th February 2026
Accepted 25th March 2026

DOI: 10.1039/d6ta01432a

rsc.li/materials-a

1. Introduction

Providing globally scalable and reliable renewable energy systems is one of the defining challenges of the 21st century. Achieving a transition from a fossil-fuel-based economy to a sustainable economy requires energy carriers and conversion technologies that can operate efficiently at scale. Over the last few decades, hydrogen has become widely recognized as an attractive energy carrier because of its high gravimetric energy density (lower/higher heating value: ~120–142 MJ kg^{-1}).[1] When produced from low-carbon electricity and used in electrochemical devices, hydrogen can enable energy conversion with water as the only direct product, offering a pathway to deep decarbonization. Two complementary technologies underpin the hydrogen energy cycle:[2] fuel cells, which convert hydrogen into electricity, and water electrolyzers, which consume electricity to split water into hydrogen and oxygen. In both devices, electrocatalysts play a decisive role in lowering kinetic barriers and improving efficiency. Commercial Pt/C catalysts are widely used to reduce overpotentials in the hydrogen evolution reaction (HER) and to enhance the oxygen reduction reaction (ORR) in fuel-cell cathodes.[3,4] Beyond fuel cells and electrolyzers, energy storage is also essential for renewable integration, and metal–air batteries (*e.g.*, Zn–air and Li–air) are particularly promising due to their high theoretical energy densities,[5] where ORR governs the discharge process at the air cathode. However, Pt is among the rarest elements in the Earth's crust, and its limited abundance and high cost remain major barriers to large-scale deployment.

To develop low-cost yet efficient electrocatalysts, it is essential to understand the relevant reaction pathways, mechanisms, and performance descriptors. In electrochemical energy-conversion and storage devices, four key half-reactions are commonly considered: the ORR, hydrogen oxidation reaction (HOR), HER, and oxygen evolution reaction (OER).[6] In fuel cells and metal–air batteries, the ORR is the cathodic reaction, whereas in water electrolyzers, the HER is a cathodic reaction. These processes have been extensively studied from both thermodynamic and kinetic perspectives, and Table 1 summarizes their key features.[3,6–10] Electrocatalytic performance is typically evaluated using metrics such as the overpotential (η), half-wave potential ($E_{1/2}$), and Tafel slope. The overpotential is the additional potential beyond the equilibrium value required to drive a desired current density;[11] η_{10} (at 10 mA cm^{-2}) is commonly used as a benchmark. The half-wave potential, $E_{1/2}$, is the potential at which the current reaches half of the diffusion-

[a]NOMATEN Centre of Excellence, National Centre for Nuclear Research, Otwock 05-400, Poland. E-mail: wenyi.huo@ncbj.gov.pl

[b]Department of Chemistry, University of Helsinki, A.I. Virtasen Aukio 1, PO Box 55, N0014, Helsinki, Finland. E-mail: pedro.camargo@helsinki.fi

[c]State Key Laboratory of Advanced Environmental Technology, Institute of Urban Environment, Chinese Academy of Sciences, Xiamen 361021, China. E-mail: bweng@iue.ac.cn

[d]University of Chinese Academy of Sciences, Beijing 100049, China

† These authors contributed equally to this work.

Table 1 Overpotentials, kinetics and benchmark catalysts for the ORR, OER, HER, and HOR[3,6–10]

Reaction	Medium	η_{10}	Kinetics	Benchmark catalysts	Comments
ORR	Acidic	~350–400 mV	Sluggish	Pt/C	$E_{1/2}$: ~0.85–0.90 V (*vs.* RHE)
	Alkaline	~300–350 mV	Slow		Kinetics better than acidic medium
OER	Acidic	~300–350 mV	Sluggish	IrO_2/RuO_2	Catalyst stability in acidic environment is low
	Alkaline	~200–270 mV	Slow	NiFe-LDH/$NiFeO_x$	
HER	Acidic	<10 mV	Fast	Pt/C	Almost no energy barrier
	Alkaline	~30–50 mV	Slow		Limited by Volmer step
HOR	Acidic	<5 mV	Fast	—	

limited value in a voltametric wave;[12] for ORR, a more positive $E_{1/2}$ generally indicates higher activity. The Tafel slope relates the overpotential to the current density[13] and provides insight into the apparent reaction kinetics and mechanistic regime.

1.1 HER pathways

The HER proceeds through adsorption and desorption steps, where * denotes an active surface site.[7] In acidic media, protons are supplied directly:

Volmer step (adsorption):

$$H^+ + e^- + * \rightarrow H^*, \quad (1)$$

Heyrovsky step (desorption):

$$H^* + H^+ + e^- \rightarrow H_2 + *, \quad (2)$$

Tafel step (desorption):

$$2H^* \rightarrow H_2 + 2^*, \quad (3)$$

In alkaline media, the source of H* is water dissociation, which typically introduces an additional kinetic barrier and slows the overall reaction:

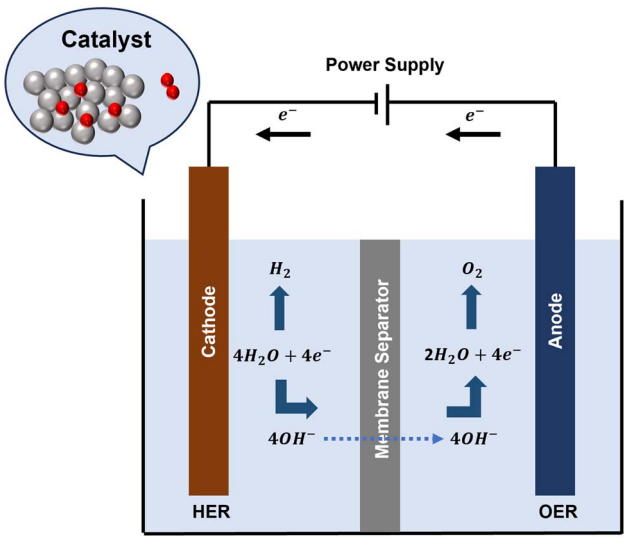

Fig. 1 Schematic diagram of water electrolysis and HER in alkaline media.

Volmer:

$$H_2O + e^- + * \rightarrow H^* + OH^-, \quad (4)$$

Heyrovsky:

$$H_2O + H^* + e^- + * \rightarrow H_2 + OH^- + *, \quad (5)$$

Tafel:

$$2H^* \rightarrow H_2 + 2^*, \quad (6)$$

Fig. 1 schematically illustrates an alkaline water electrolyzer. According to the Sabatier principle, an effective HER catalyst should exhibit intermediate binding strength toward adsorbed hydrogen (H*).[14] If H* binds too weakly, the reaction is limited by the adsorption/activation step (Volmer), whereas overly strong binding hinders H_2 formation and release *via* the Heyrovsky or Tafel steps. This balance is captured by the HER volcano plot, where Pt is located near the apex,[4] which is consistent with its near-thermoneutral hydrogen adsorption free energy (ΔG_{H^*} close to 0).

1.2 ORR pathways

The ORR can proceed *via* two-electron or four-electron pathways.[15] The four-electron ORR is the desired route for fuel cells and metal–air batteries because it maximizes energy efficiency and yields H_2O (acidic) or OH^- (alkaline) as the final product. Fig. 2 shows a schematic diagram of a fuel cell in an acidic environment. The elementary steps differ between acidic and alkaline media due to the availability of H^+.

In acidic media, H^+ is provided:

$$O_2 + H^+ + e^- \rightarrow OOH^*, \quad (7)$$

$$OOH^* + H^+ + e^- \rightarrow O^* + H_2O, \quad (8)$$

$$O^* + H^+ + e^- \rightarrow OH^*, \quad (9)$$

$$OH^* + H^+ + e^- \rightarrow H_2O, \quad (10)$$

In alkaline environments, due to the lack of H^+, the specific reaction pathways are different. This results in different overpotentials and reaction kinetics.

$$O_2^* + H_2O + e^- \rightarrow OOH^* + OH^-, \quad (11)$$

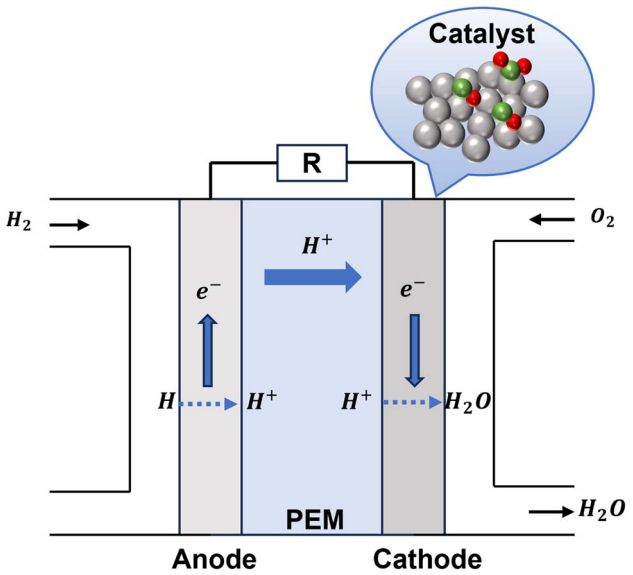

Fig. 2 Schematic diagram of the fuel cell and ORR in acidic media.

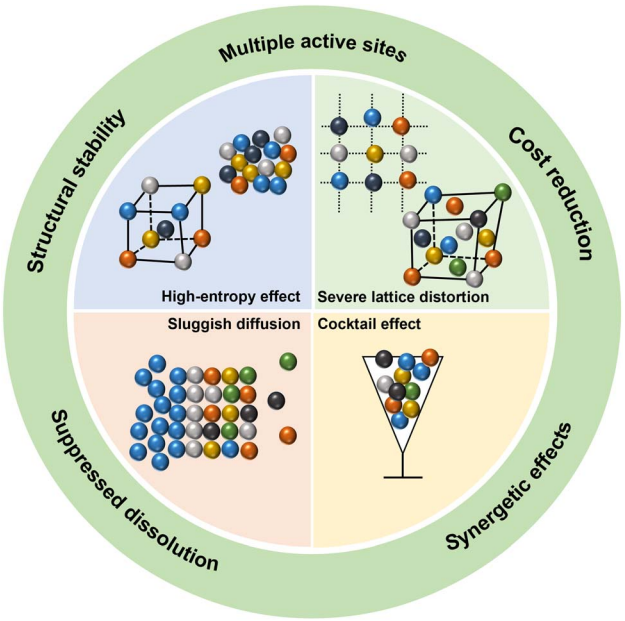

Fig. 3 Four core effects of HEAs.

$$OOH^* + e^- \rightarrow O^* + OH^-, \quad (12)$$

$$O^* + H_2O + e^- \rightarrow OH^* + OH^-, \quad (13)$$

$$OH^* + e^- \rightarrow * + OH^-, \quad (14)$$

The corresponding anodic/counter reactions are closely linked: HOR is the reverse of HER, and OER is the reverse of ORR.[6] For acidic OER, IrO_2/RuO_2 are commonly used benchmarks,[7] although acidic environments can accelerate dissolution and structural degradation.

1.3 Motivation for HEAs and core effects

To reduce cost while enabling large-scale applications, intensive efforts have focused on increasing the intrinsic catalytic activity and active-site density, lowering platinum group metals (PGMs) content, and improving stability. High-entropy alloys (HEAs) have attracted considerable attention because their multielement compositions can provide diverse local environments and tunable electronic structures. Four commonly discussed core effects of HEAs are the high-entropy effect, sluggish diffusion, severe lattice distortion, and the cocktail effect.[16] Fig. 3 summarizes these concepts and their relevance for electrocatalyst design.

The high-entropy concept originates from the configurational mixing entropy of multicomponent alloys, defined as follows:

$$\Delta S_{mix} = -R\sum_{i=1}^{n} c_i \ln c_i \quad (15)$$

where R is the gas constant, c_i is the molar fraction of element i, and n is the number of constituent elements.

High ΔS_{mix} reduces the Gibbs free energy ΔG_{mix} and drives the formation of solid-solution structures, such as face-centered cubic (FCC) and body-centered cubic (BCC) structures.[17] This offers a framework for accommodating multiple active-site motifs within a single lattice and for accessing wide compositional spaces that may reduce noble-metal dependence and cost.[18] Large atomic-size mismatch and diverse chemical interactions can induce lattice distortion,[19] which may shift the d-band center and modify the local density of states,[20] thereby influencing adsorption energetics and reaction barriers. In addition, sluggish diffusion arising from complex energy landscapes can reduce atomic mobility,[16] which may help suppress segregation, dissolution, and phase transformation during long-term electrochemical operation.[21] Finally, the cocktail effect reflects emergent synergistic properties that arise from multielement interactions,[16] including charge redistribution, work-function variation, and diverse coordination environments, which together can further tune adsorption energies and catalytic kinetics.

With the reaction fundamentals and key evaluation metrics established above, the next step is to contextualize how the HEA electrocatalysis field has evolved and where current emphasis lies. Accordingly, this review begins with a bibliometric analysis to map keyword and citation networks, highlighting dominant reactions, material motifs, and emerging computational/design themes. We then classify reported HEA catalysts for ORR and HER according to composition and electronic-structure characteristics (3d/4d/5d transition-metal dominance), and summarize representative synthetic strategies alongside structure–property considerations. Finally, we discuss remaining challenges, including benchmarking, identification of the true active state under operating conditions, device-level translation, scalability, and sustainability, and provide an outlook toward practical electrochemical applications.

2. Bibliometric analysis

Analyzing the co-occurrence and co-evolution of keywords in the literature can reveal emerging priorities and research directions

within a field. Here, a bibliometric analysis was performed based on the Web of Science (WoS) Core Collection, and VOSviewer was used for data processing, network construction, and visualization.[22]

Among the four half reactions, HER, OER and ORR have been intensively studied, while HOR has been investigated much less. The ORR and OER have intrinsically sluggish multistep kinetics. The HER plays a central role in green hydrogen production. All of these compounds have both scientific and commercial value. The relatively low bibliometric prominence of HOR does not imply limited technological importance. This reflects the fact that the HOR is less frequently identified as the primary catalytic bottleneck in electrochemical devices.

The keyword network highlights a close relationship between catalyst design, reaction mechanism, and electrocatalytic performance. The reaction-related terms are strongly connected to "adsorption", "kinetics", "phase", "microstructure", "total-energy calculations", and "machine learning". Linking the local chemical environment and structural features with the adsorption behavior, reaction pathways, and final catalytic performance is important. Rational HEA design requires the combined consideration of composition, active-site heterogeneity, and mechanism-based optimization. Morphology-related terms, such as nanoparticles and nanosheets, also appear centrally in Fig. 4. This highlights the importance of controlling the nanoscale structure. Reducing the nanoparticle size generally increases the electrochemically accessible surface area and can increase the apparent activity. Size also influences stability through dissolution, aggregation, and Ostwald ripening under electrochemical operation.[23] Similarly, HEA nanosheets have been widely investigated. 2D architectures provide high surface-to-volume ratios and expose more surface/edge atoms. Ultrathin morphologies can shorten charge/ion transport pathways and increase the fraction of accessible active sites.[24] These scientific outcomes are consistent with the keyword co-occurrence map. Surface engineering, dimensional control and architectural design remain closely connected with catalytic performance in HEA electrocatalysis. From an elemental perspective, 3d transition metals, *e.g.*, Fe, Co, Ni, and Cu, occur most frequently. It reflects a strong motivation toward cost reduction and electronic structure tuning.

The VOSviewer clustering algorithm assigns colors to groups of keywords that exhibit stronger internal connectivity, *i.e.*, tighter co-occurrence patterns. The red cluster is dominated by

Fig. 4 Keyword co-occurrence analysis. Dataset: WoS Core Collection. Keywords: "high-entropy alloy" and "catalysis". Data visualization: VOSviewer.[22]

"hydrogen evolution reaction", "oxygen evolution reaction", and "water splitting", and includes support- and architecture-related terms such as "carbon", "oxides", "nanosheets", and "carbon nanotubes", indicating strong coupling between reaction studies and electrode/support engineering. The yellow cluster centers on "oxygen reduction reaction" and "performance", and appears close to "Pd", suggesting that ORR-focused HEA studies frequently involve noble-metal-containing nanoparticles. The blue cluster groups computational and data-driven terms such as "adsorption", "total-energy calculations", and "machine learning", reflecting the growing role of descriptor-based optimization and advanced modeling. The green cluster emphasizes "stability", "mechanism", "kinetics", "phase", and "microstructure", underscoring the importance of durability and structure–property relationships.

Element-specific keywords also show informative positioning. Fe, Co, and Ni appear frequently and are closely associated with "stability" and "mechanism", which is consistent with the prevalence of 3d-rich HEAs aimed at robust surfaces and multisite chemistry. Cu co-occurs with terms such as "adsorption" and "transition", suggesting roles in electronic tuning and model-guided design. In contrast, Pt and Pd appear closer to ORR- and oxidation-related terms, which is consistent with their role as highly active components in high-performance electrocatalysts.

3. HEA performance in terms of ORR/HER

3.1 Classification based on the d-block period

To discuss the catalytic performance of HEAs in the ORR and HER, they are classified into 3d-, 4d-, and 5d-transition-metal (TM)-based groups according to the dominant d-block period (3d: Sc–Zn; 4d: Y–Cd; 5d: Hf–Hg). This classification is not just used for a clear compositional design. It can reflect the linkages and trends from periodic trends and electronic structure to adsorbate binding and reaction kinetics. Elemental contributions were weighted by the atomic fraction (at%), and the fractions from 3d, 4d, and 5d elements were summed. A catalyst is assigned to a given category when one d-series accounts for >50 at% of the total composition. For example, CoCrFeMnNi is a representative 3d-TM-based HEA, whereas $Pt_{28}Mo_6Pd_{28}Rh_{27}Ni_{15}$ is classified as 4d-TM-based because Mo, Pd, and Rh together contribute 61 at%, with Pt as 5d and Ni as 3d. Catalysts that do not show clear dominance by a single d-series, or that contain substantial non-TM components, are grouped as others, *e.g.*, PdPtRhIrCu, where 4d and 5d fractions are comparable and 3d elements also contribute.

Electronic properties, such as the d-band width, d-band filling of the active center and neighborhood electronegativity, can influence the electrocatalytic performance of HEAs.[25] They cause charge redistribution and different energy barriers for reaction intermediates. Across the 3d, 4d and 5d series, d orbitals become more spatially extended, which can influence metal-adsorbate interactions. 3d elements have more localized d states and narrower d bands. This leads to stronger adsorption to oxygenated intermediates. This can facilitate O_2 activation or H_2O dissociation, but it can also hinder the removal of OH* when adsorption becomes excessive. Qian *et al.* applied density functional theory (DFT) calculations to investigate the water and hydrogen interactions on CoCrFeMnNi.[26] The catalyst followed a dominant four-electron ORR pathway. O* and OH* adsorption strongly depends on the local binding atom, with a clear preference for Cr-containing sites. 4d-TM-based HEAs contain more spatially extended d orbitals and broader d bands. Their electronic states are less localized. The adsorption strength of intermediates is often more balanced. The optimum for HEAs does not necessarily require one uniform site with $\Delta G_{H^*} = 0$.[27] This is particularly beneficial for the HER. Li *et al.* applied DFT calculations and *operando* XAS to investigate the hydrogen evolution mechanism on PdRhMoFeMn high-entropy metallenes.[28] The catalyst showed high HER activity in acidic, neutral, and alkaline media. Rh sites are responsible for favorable hydrogen adsorption. Pd sites facilitate H_2O adsorption/dissociation. The Fe and Mn sites stabilize the hydroxide ions. They synergistically promote overall HER kinetics. Compared with 3d- and 4d-rich HEAs, 5d-TM-based HEAs present more spatially extended d orbitals and stronger relativistic effects. This allows more delicate tuning of the local electronic structure and binding of key oxygenated intermediates. Within the Hammer–Nørskov d-band framework, a higher d-band center (closer to the Fermi level) generally strengthens chemisorption by reducing antibonding-state occupation, whereas a downshift of the d-band center increases antibonding filling and weakens the metal–adsorbate bond (Fig. 5a).[29,30] Consistent with this picture, Fig. 5b shows an approximately linear correlation between the hydrogen adsorption potential (*E vs.* SCE) and the calculated d-band shift ($\delta_{\varepsilon d}$) for Pd monolayers on different single-crystal substrates.[30] Such scaling trends provide a useful starting point for rationalizing composition–activity relationships in HEA electrocatalysts. Notably, in HEAs the near-surface composition can evolve under bias, so electronic descriptors should ideally be interpreted alongside *operando* or post-test surface characterization.

Beyond the general d-band center trend, mixing elements from different d-block rows introduces additional electronic effects, enabling unique catalytic performance capability.[33–35] The 4d and 5d orbitals are more radially extended than 3d is. The increased orbital overlap broadens the d-band and shifts the band center downward, consequently weakening the adsorption capacity. However, local chemical disorders in HEAs usually contribute to a spectrum of coordination environments rather than single band center values.[36] This yields a heterogeneous ensemble of adsorption sites that collectively spans the optimal binding energy window for a given reaction, which is a key distinction from conventional binary or ternary alloys.[37] Distinct d-orbital overlaps among the constituent metals increase the electron density near the Fermi level and produce a distribution of active-site adsorption energies, indicating that the performance of these materials is superior to that of binary analogs.[38] The pronounced difference in spin–orbit coupling strength introduces further complexity in 3d–5d mixed systems. Strong spin–orbit coupling in 5d metals can partially increase orbital degeneracies and alter the local density of states (LDOS)

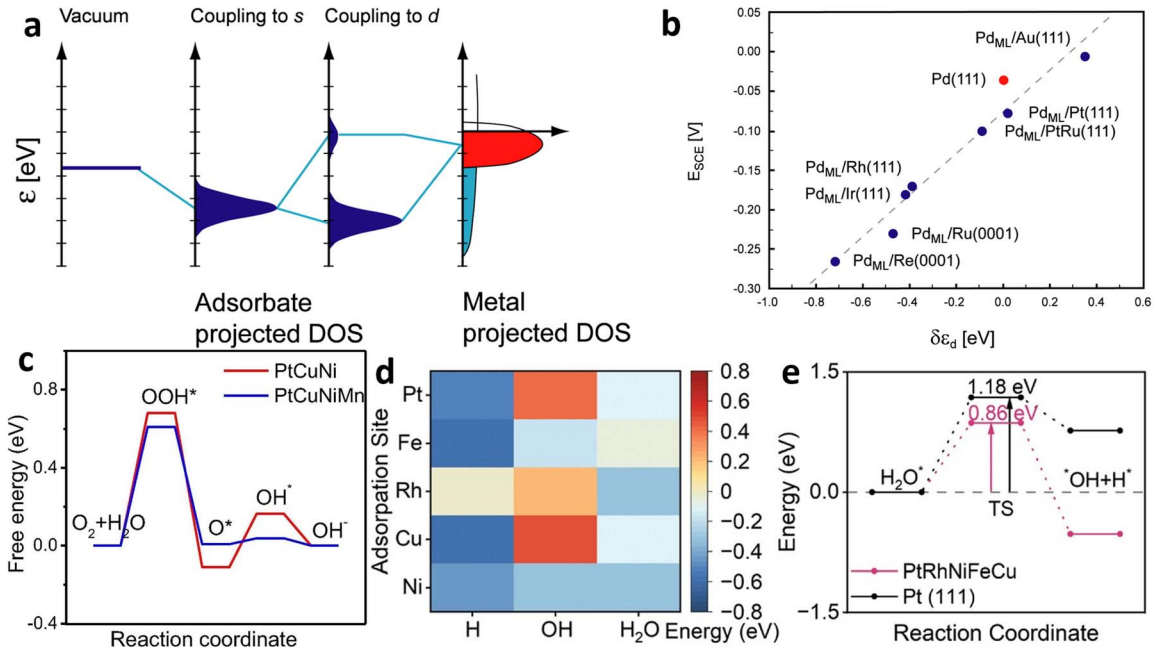

Fig. 5 (a) Schematic illustration of bond formation between the valence level and the s and d states of a TM surface. Reproduced with permission.[29] Copyright 2011, National Academy of Science, USA. (b) Electrochemically measured changes in the hydrogen adsorption energy (E_{SCE}) are shown to scale well with the calculated shift in the d-band center ($\delta_{\varepsilon d}$). Adapted with permission.[29] Copyright 2011, National Academy of Science, USA. Reproduced with permission.[30] Copyright 2005, Wiley-VCH GmbH. (c) Free energy profiles for various ORR steps with the CuNiMnPt and CuNiPt catalysts. Reproduced with permission.[31] Copyright 2020, Elsevier. (d) Adsorption preferences for water and intermediates on different metal sites of the HEA. (e) Activation energies of water dissociation of PtRhNiFeCu and Pt. Reproduced with permission.[32] Copyright 2024, Wiley-VCH GmbH.

near the Fermi level. Cross-period orbital energy alignment has been shown to induce strong exchange-type interactions that govern both the electronic structure and functional properties under elevated conditions.[39] Electronegativity and work function differences between 3d and heavier-period components also drive local charge redistribution.[40] These considerations suggest that the d-band width, LDOS shape, spin–orbit coupling, and cross-series charge transfer should all be considered alongside the d-band center when interpreting the catalytic behavior of HEAs spanning multiple d-block rows.

3.2 3d transition-metal (TM)-based HEAs

3d transition metals (TMs) include earth-abundant elements such as Fe, Co, Ni, Mn, and Cr. They are important in the rational design of HEA electrocatalysts because of their cost-effectiveness and distinct electronic configurations. In the ORR, oxygenated intermediates, such as OH* and O*, have high adsorption energies with Pt and hinder the reaction kinetics.[41] The incorporation of 3d TMs into noble-metal lattices can downshift the d-band center and lower the adsorption energy.[42] During the alkaline HER, the kinetics of water dissociation (Volmer step) are sluggish. Oxyphilic 3d TMs can lower the energy barrier and accelerate the overall reaction rate.[43]

He *et al.* synthesized CoCrFeMnNi alloys as ORR catalysts in alkaline media *via* a solution-based approach.[44] The catalyst showed an onset potential of 0.88 V and a half-wave potential of 0.78 V *vs.* RHE. These performances are comparable to those of a commercial Pt/C benchmark. Li *et al.* used a top-down strategy to fabricate an Al–Cu–Ni–Pt–Mn nanoporous HEA.[31] The Pt content is less than 30 at%. The catalyst reached a half-wave potential of 0.945 V in 0.1 M $HClO_4$. The surface activity (5.5 mA cm^{-2}) is 16 times greater than that of Pt/C. The catalyst remained stable for 164 h at 0.7 V. The authors further investigated the effect of Mn *via* first-principles calculations. Fig. 5c shows the free energy profiles of each ORR step on CuNiMnPt and CuNiPt. Mn altered the OOH* adsorption geometry and reduced the overpotential. Wang *et al.* reported carbon-supported $Pt_{21}Fe_{20}Co_{20}Ni_{20}Mn_{19}$ NPs for the ORR.[45] The catalyst reached a half-wave potential of 0.88 V in acidic media. The specific activity reached 2.84 mA cm_{Pt}^{-2} at 0.9 V, which is much higher than that of Pt/C. Hu *et al.* synthesized ultrasmall PtRhNiFeCu HEA NPs with a single-phase FCC structure.[32] Fig. 6e showed the comparison of overpotential and Tafel slope between this catalyst and other common HEAs. The catalyst delivered great catalytic activity for both the ORR and HER. For the acidic ORR, the mass activity reached 1.23 A mg_{Pt}^{-1} at 0.9 V. The specific activity reached 2.67 mA cm_{Pt}^{-2} at 0.9 V. The catalyst also delivered an overpotential of 13 mV at 10 mA cm^{-2} in 1 M KOH. They further conducted DFT calculations to investigate the mechanisms involved. The synergetic effects between the 3d TM components and Pt/Rh decrease the energy barrier for water dissociation and enhance hydrogen adsorption, as shown in Fig. 5d and e. Chen *et al.* designed a structurally ordered high-entropy intermetallic for practical fuel

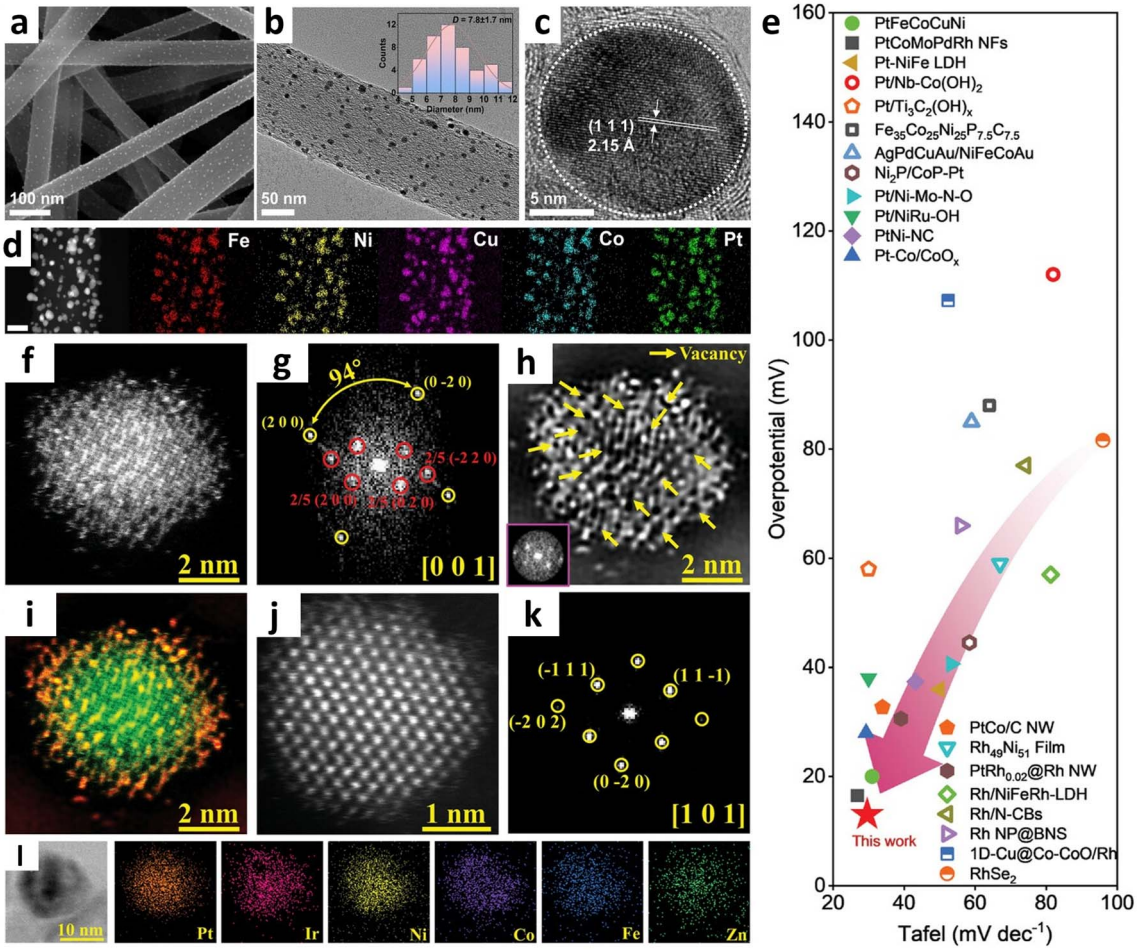

Fig. 6 (a)–(d) Scanning electron microscope (SEM), transmission electron microscope (TEM), high resolution TEM (HRTEM), high-angle annular dark-field scanning TEM (HAADF-STEM) images and energy dispersive spectroscopy (EDS) mapping of FeNiCuCoPt on carbon nanofibers. (Scale bar in (d): 50 nm). Reproduced with permission.[48] Copyright 2024, Wiley-VCH GmbH. (e) Overpotentials at 10 mA cm^{-2} and Tafel slopes for various HEAs for the alkaline HER. Reproduced with permission.[32] Copyright 2024, Wiley-VCH GmbH. (f) HR-STEM image of a PtIrNiCoFeZn HEA nanoparticle. (g) Fast Fourier transform (FFT) pattern of (f). (h) Inverse FFT (IFFT) image of the corresponding FFT pattern (inset). (i) Color-mixed images of (f) and (h); (f) is set as green, and (h) is set as red. (j) HR-STEM image of a PtIrNiCoFe HEA nanoparticle. (k) FFT pattern of (j). (l) STEM-EDS mapping of a PtIrNiCoFeZn HEA. Reproduced with permission.[49] Copyright 2024, Wiley-VCH GmbH.

cells.[46] The PtZnFeCoNiCr high-entropy intermetallic NPs showed a half-wave potential of 0.948 V in acidic media. The mass activity reached 4.12 A mg_{Pt}^{-1} at 0.90 V. The half-wave potential decay was very low (7 mV) after 20 000 cycles. When put into a proton-exchange membrane fuel cell, the catalyst delivered a peak power density of 1.9 W cm^{-2} with low Pt loading. Madan *et al.* reported a nanocrystalline CuCoMnNiFe HEA for use in zinc–air batteries.[47] The catalyst acted as a bifunctional oxygen electrocatalyst in an alkaline electrolyte. The ORR onset potential reached 0.78 V *vs.* RHE. The ORR overpotential was reported to be 120 mV higher than that of Pt/C in the same test set. Pan *et al.* accelerated composition discovery *via* high-throughput electrochemical screening.[48] The discovery methodology combined scanning electrochemical cell microscopy (SECCM) screening with rapid synthesis of Pt-based HEA catalysts. They identified the FeNiCuCoPt HEA supported on carbon nanofibers as a top-performing composition. Fig. 6a–d show the morphologies and characteristic lattice spacings. The catalyst reached a half-wave potential of 0.892 V in an acidic environment. The mass activity reached 1.32 A mg_{Pt}^{-1} at 0.85 V. The half-wave potential decay was approximately 10 mV after 10 000 cycles.

In alkaline media, 3d TMs provide oxyphilic sites for H_2O and OH*. They can lower the energy barrier for the water dissociation step. Huang *et al.* prepared lattice-disordered PtIrNiCoFeZn HEA NPs for the HER.[49] This HEA has a single-phase face-centered cubic structure. The lattice structure is highly disordered with respect to the observed defects, as shown in Fig. 6f–l, which resulted in delivered an overpotential of 10 mV at 10 mA cm^{-2} in 1 M KOH. The Tafel slope reached 16.9 mV dec^{-1}. DFT calculations further support the enhanced reaction kinetics. Vacancies in this highly disordered HEA accelerate both the Volmer and Tafel steps. Wang *et al.* designed Ru-doped (0.2 at%) $Pt_{24.8}Fe_{12.7}Ni_{7.1}Cu_{34.5}W_{20.8}$ HEA nanocrystals on carbon nanotubes.[50] The octahedral morphology enriched well-defined facets and stabilized active ensembles under operation, as shown in Fig. 7a–c. The catalyst delivered 9 mV at 10 mA

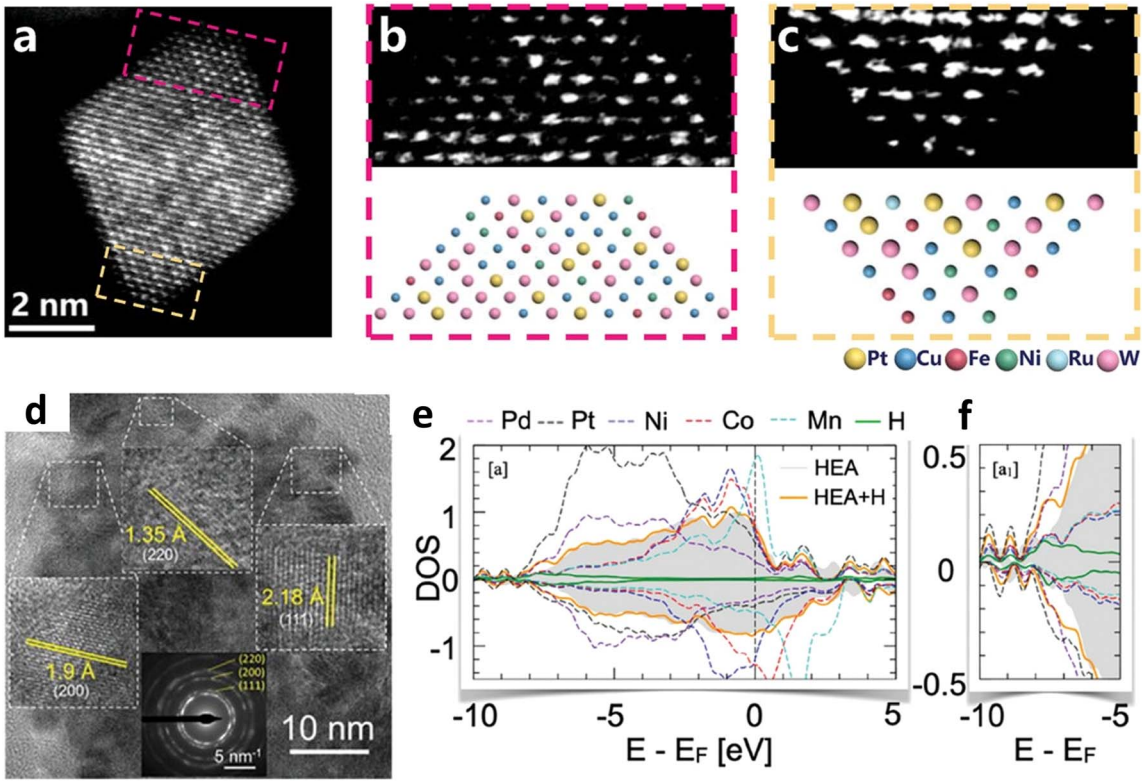

Fig. 7 (a)–(c) HAADF-STEM image and atomically resolved HAADF-STEM images of Ru-doped (0.2 at%) $Pt_{24.8}Fe_{12.7}Ni_{7.1}Cu_{34.5}W_{20.8}$ HEA nanocrystals. Corresponding simulated atomic images contained in (b) and (c). Reproduced with permission.[50] Copyright 2024, Wiley-VCH GmbH. (d) HRTEM image showing the *d*-spacing value of PtPdNiCoMn. (e) and (f) DFT calculation of the PDOS of PtPdNiCoMn and the magnified region. Reproduced with permission.[53] Copyright 2025, Wiley-VCH GmbH.

cm^{-2} in 0.5 M H_2SO_4 and 16 mV at 10 mA cm^{-2} in 1.0 M KOH. It can also sustain long-term operation at high current density. Ru doping enhanced the concurrent reduction and HEA nanocrystal growth. Chen *et al.* achieved one-pot growth of convex cube $Pt_{34}Fe_5Ni_{20}Cu_{31}Mo_9Ru$ HEA nanocrystals.[51] The particles exposed facets and used Ru to direct shape evolution. The catalyst delivered an overpotential of 20 mV at 10 mA cm^{-2} in the alkaline HER. The same material also supported multifunctional electrocatalysis. Sivanantham *et al.* synthesized single-phase FCC $V_xCuCoNiFeMn$ HEAs ($x = 0$, 0.5, 1) *via* high-energy ball milling.[52] The equiatomic VCuCoNiFeMn had $\eta_{50} =$ 250 mV and a Tafel slope of 148 mV dec^{-1} in 1 M KOH. The electrode remained stable for >20 h at 50 mA cm^{-2}. Chandran *et al.* designed a PtPdNiCoMn HEA *via* a descriptor-guided screening scheme and synthesized it *via* electrodeposition.[53] The product formed a phase-pure FCC. Fig. 7d shows the *d*-spacing value and the SAED pattern. The catalyst delivered an overpotential of 22.6 mV at 10 mA cm^{-2} in alkaline electrolyte. It also maintained operation at 100 mA cm^{-2} for 100 h. DFT calculations revealed a near-zero Gibbs formation enthalpy for the PtPdNiCoMn HEA. The calculated projected density of states (PDOS) for the HEA revealed weak coupling between the H-1s states and TM-d states, as illustrated in Fig. 7e and f. Strong coupling was observed at lower energies (−6 to −8.5 eV), which are below the Fermi level.

3.3 4d transition-metal-based HEA

Two typical 4d TM-based HEAs are the Ir–Pd–Pt–Rh–Ru and Ag–Ir–Pd–Pt–Ru systems. Noble PGMs, such as Pd, Rh and Ru, tune the adsorption of O* and OH* toward the volcano optimum.[54] 4d orbitals are more spatially extended than 3d orbitals are. Alloy hybridization can downshift the surface d-band center and weaken the binding of oxygenated intermediates on Pt or Ir.[35] The increased orbital overlap in 4d-rich HEAs also broadens the d-band width and generates a wider distribution of local adsorption energies across surface sites. The d-electron self-complementation effect among constituent 4d metals has been shown to increase the electron density near the Fermi level and upshift the overall d-band center relative to that of binary counterparts, directly lowering the energy barrier for intermediate transfer during catalysis.[38,55] Batchelor *et al.* built a DFT adsorption database for Ir–Pd–Pt–Rh–Ru and Ag–Ir–Pd–Pt–Ru.[56] They combined DFT sampling with a site ensemble model to predict O* and OH* adsorption energies, as shown in Fig. 8a and b. The composition and resulting overpotential can then be optimized. Fig. 8c–f show the adsorption energy distributions for various compositions. In the Ag–Ir–Pd–Pt–Ru system, a computational activity model coupled with the Sabatier optimum was used.[57] The FCC solid-solution regions near $Ag_5Ir_5Pt_{20}Pd_{35}Ru_{35}$ (4d TM-based) and $Ag_5Ir_5Pd_{17}Pt_{68}Ru_5$ (5d TM-based) showed the highest activity. These regions surpassed a Pt

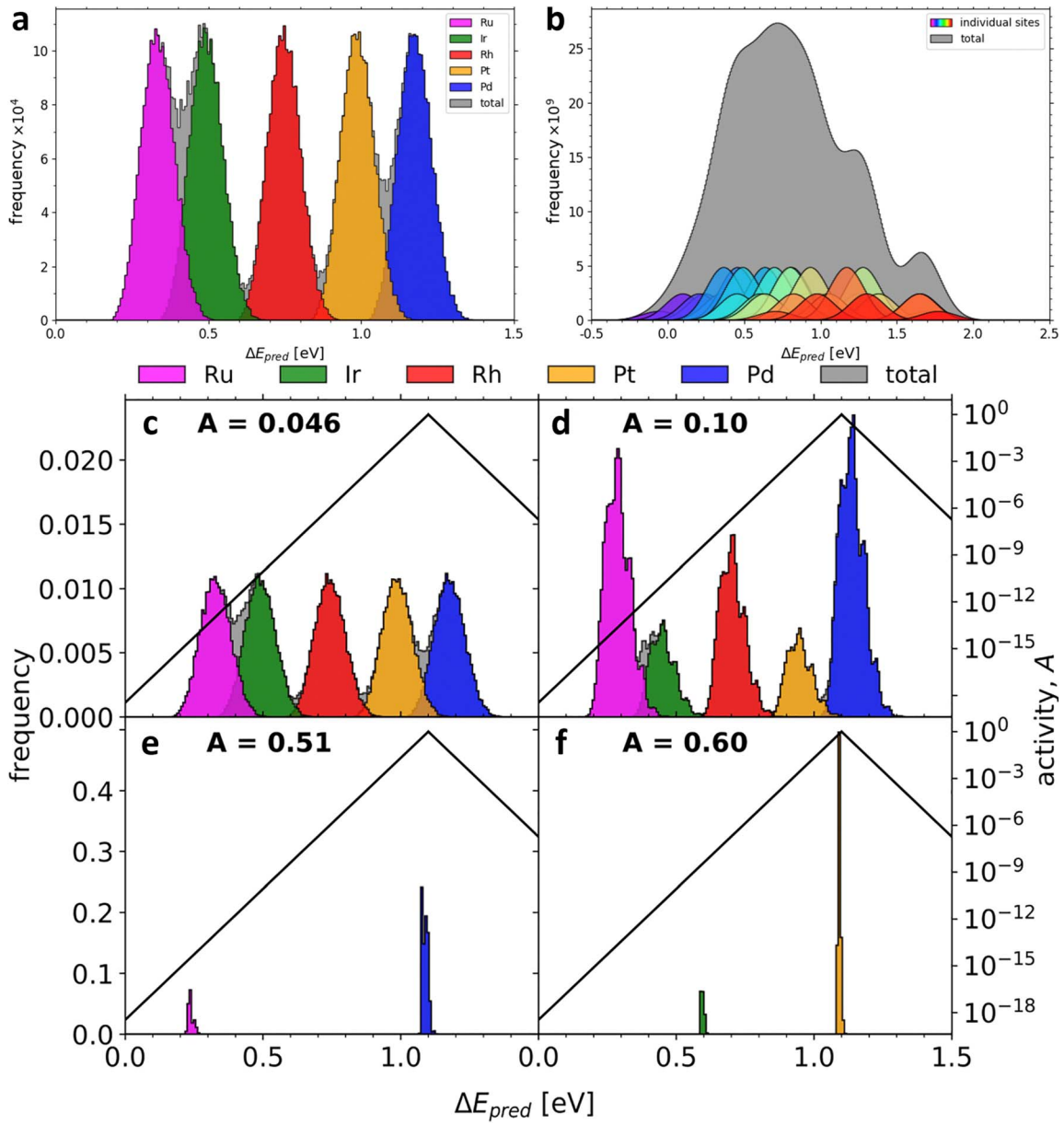

Fig. 8 (a) and (b) Predicted adsorption energies for OH* and O*. (c), (d), (e), and (f) Distributions of the adsorption energies for IrPdPtRhRu, $Ir_{10.2}Pd_{32}Pt_{9.3}Rh_{19.6}Ru_{28.9}$, $Pd_{81.7}Ru_{18.3}$ and $Ir_{17.5}Pt_{82.5}$, respectively. Reproduced with permission.[56] Copyright 2019, Cell Press.

thin-film benchmark with a strongly reduced Pt fraction. Pedersen *et al.* further applied Bayesian optimization to a DFT-based activity model.[58] They validated the predictions on thin-film spreads. The search highlighted activity hot spots near $Ag_{14}Pd_{86}$, $Pd_{65}Ru_{35}$, and $Ir_{35}Pt_{65}$ under the same testing protocol. Xu *et al.* used multiobjective Bayesian optimization for ORR catalyst discovery.[59] They optimized the activity, cost, and entropic stabilization at the same time. A graph neural network was used to train the DFT adsorption enthalpy database. They screened composition spaces with up to 10 elements and identified many optimal ORR catalyst candidates to balance performance and synthesizability.

In 4d TM-based HEAs, Ru/Rh/Pd/Mo broadens the surface d-states and generates varied local electronic environments. The surface therefore presents a distribution of ΔG_{H^*} and Volmer barriers across different active sites.[60] The composition optimizes the H* adsorption sites and reduces the required overpotential. The catalytic activity varied with different pH values and synthetic routes. Wu *et al.* synthesized IrPdPtRhRu HEA NPs *via* a one-pot polyol process.[61] In an acidic environment, they reported a turnover frequency (TOF) of 0.054 s^{-1} at a 25 mV overpotential, which is much higher than that of commercial Pt/C at the same potential. Kang *et al.* synthesized PtPdRhRuCu mesoporous nanospheres with a core–shell structure.[62] The polycrystallinity and mesoporous morphologies are shown in Fig. 9a–c. The catalyst showed great HER catalytic activity in all the tested pH environments. It reached η_{10} = 10 mV in 1.0 M KOH, η_{10} = 13 mV in 0.5 M H_2SO_4, and η_{10} = 28 mV in 1.0 M

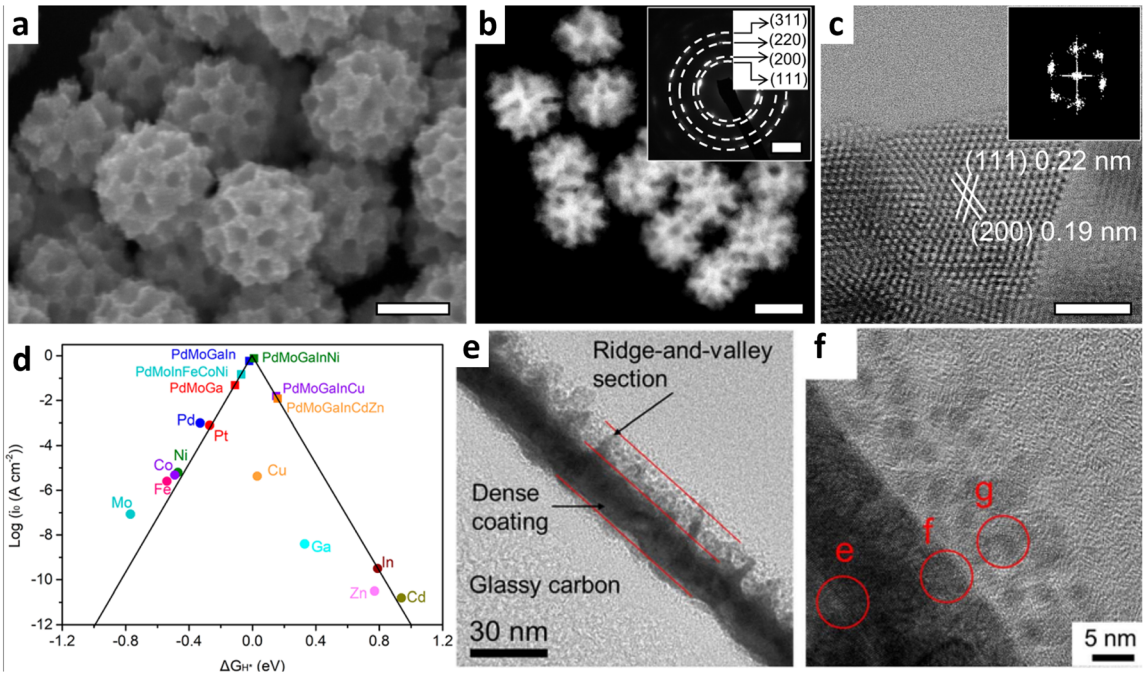

Fig. 9 (a) SEM image (scale bar: 100 nm) and (b) HAADF-STEM image (scale bar: 100 nm). Insets: corresponding SAED patterns (scale bar: 5 nm^{-1}). (c) HRTEM (scale bar: 2 nm) (FFT patterns are shown in the inset) of the PtPdRhRuCu mesoporous nanospheres. Reproduced with permission.[62] Copyright 2023, Springer Nature. (d) A plot constructed from experimentally derived exchange current densities and computationally calculated hydrogen binding energies of various single elements and HEAs. Reproduced with permission.[65] Copyright 2022, American Chemical Society. (e) and (f) HR-TEM images of the cross-sectional and subsurface areas of $Ir_{20.3}Pd_{16.3}Pt_{8.6}Rh_{26.1}Ru_{28.7}$/GC. Reproduced with permission.[66] Copyright 2024, Royal Society of Chemistry.

phosphate-based saline (PBS). This revealed that the synergetic effect from highly entropic active metal sites can accelerate HER kinetics. Yu *et al.* prepared IrPdPtRhRu HEA NPs *via* a laser-thermal reduction route.[63] The catalyst achieved $\eta_{10} = 12$ mV in 0.5 M H_2SO_4, $\eta_{10} = 16$ mV in 1.0 M KOH, and $\eta_{10} = 28$ mV in alkaline simulated seawater. The catalyst also showed great stability in the alkaline HER (>2000 cycles). Wei *et al.* designed a $Pt_{28}Mo_6Pd_{28}Rh_{27}Ni_{15}$ HEA nanocrystal with radial nanosheets and strong d–d electron interactions.[64] The catalyst delivered a low overpotential of 9.7 mV at −10 mA cm^{-2} in an alkaline environment. Fu *et al.* optimized the hydrogen binding energy and designed a Pt-free composition PdMoGaInNi.[65] Fig. 9d shows the computational prediction of ΔG_{H^*} for various HEA compositions. Experimentally, the 2D PdMoGaInNi nanosheets delivered $\eta_{10} = 13$ mV in 0.5 M H_2SO_4 and were sustained for 200 h at 100 mA cm^{-2} in a PEM water electrolyzer. Zou *et al.* fabricated $Ir_{20.3}Pd_{16.3}Pt_{8.6}Rh_{26.1}Ru_{28.7}$ HEA thin films on glassy carbon *via* sequential atomic layer deposition with electrical Joule heating.[66] The surface microstructure is a mixture of nanocrystalline and amorphous structures, as shown in Fig. 9e and f. This can be attributed to the crystallization process during Joule heating (1000 °C, 5 s). The fabricated catalyst achieved overpotentials of 13 mV at 10 mA cm^{-2} in 0.5 M H_2SO_4, 77 mV in PBS, and 65 mV in 1.0 M KOH. DFT further supported this electrocatalytic performance. These findings indicate that the surface–hydrogen interaction at the amorphized interface was strengthened. Huang *et al.* synthesized disordered PtRhPdIrRu HEA nanoparticles under vigorous boiling and achieved a TOF of 33.1 s^{-1} at 50 mV in acid, which is 5.4 times greater than that of Pt.[67] They highlighted disorder-enabled local electronic states and improved noble metal utilization.

3.4 5d transition-metal-based HEAs and others

Compared with 3d- and 4d-TM-based HEAs, 5d-TM-based HEAs are less investigated due to their cost inefficiency. However, they still exhibit greater catalytic performance at a lower cost than Pt does. Owing to the four core effects of HEAs, they normally exhibit more active sites, leading to higher catalytic activity and greater stability. Chen *et al.* fabricated nanoporous PtRuCuOsIr for the acidic ORR.[68] The half-wave potential reached 0.900 V *vs.* RHE, which is higher than that of commercial Pt/C catalysts. The mass activity and specific activity are 1.6 and 3.8 times greater, respectively, than those of Pt/C. The activity loss remained small after 15 000 potential cycles. Pittkowski *et al.* synthesized $Ru_{11}Rh_{26}Os_6Ir_{22}Pt_{35}$ HEA NPs from single-source precursors and reduced them at moderate temperatures.[69] Compared with Pt, the catalyst improved the ORR performance. They further investigated the phase formation of the Pt–Ir–Os–Rh–Ru system. The inhibition of precursor mobility can favor solid-solution formation. The content of Rh also matters; $Ru_{11}Rh_{26}Os_6Ir_{22}Pt_{35}$ is FCC, and $Ru_{31}Rh_9Os_{30}Ir_{15}Pt_{15}$ is HCP.

Mixing 3d-, 4d-, and 5d-TM elements with similar atomic ratios is also an efficient strategy. It allows precise electron regulation across mixed noble and nonnoble motifs. Mao *et al.* synthesized an ultrathin PdPtRhIrCu HEA metallene.[70] The large atomic differences produce severe lattice distortions. It delivered $\eta_{10} = 15$

mV in 1 M KOH. The Tafel slope was 37 mV dec^{-1}. Feng *et al.* constructed NiCoMoPtRu HEA nanoclusters on carbon.[71] The nanoclusters approached an average size of 1.48 nm (7 atomic layers). It reached an overpotential of 9.5 mV in 1 M KOH. The Tafel slope was 29.8 mV dec^{-1}. The mass activity reached 3314.3 A g at 70 mV. This work also demonstrated hydrazine oxidation-assisted hydrogen production. The cell voltage reached 141 mV at 10 mA cm^{-2}. Cai *et al.* reported size-dependent HER on PtRuPd-CoNi HEA nanoparticles.[72] The 1.7 nm sample reached 16 mV in 1 M KOH. The mass activity reached 31.9 A mg at 100 mV. This work linked the enhanced HER to higher fractions of undercoordinated sites. It also linked the enhanced HER to a more favorable adsorption-energy distribution at smaller sizes. Wang *et al.* applied a step-alloying strategy for synthesizing ultrahigh-component HEA nanoparticles.[73] Pt-rich seeds were used in the first step. The composition incorporated strongly repellent element pairs. The 14-element composition (3d: 4, 4d: 5, 5d: 5) reached $E_{1/2} = 0.86$ V in 0.1 M KOH. This demonstrated the practical expansion of the ORR compositional space. The results also revealed stable solid-solution formation with high mixing entropy. Chen *et al.* fabricated an acanthosphere-like PtRuRhPdAuIr HEA *via* electrodeposition.[74] The acanthosphere morphology increased the accessible surface area and exposed multiple active sites. The catalyst delivered $\eta_{10} = 16$ mV in acidic media and 74 mV in alkaline media. Tong *et al.* designed IrRuMoWCu HEA NPs on N-doped nanospheres.[75] The structure creates near-continuous adsorption energies of O* and OH*. The catalyst achieved $\eta_{10} = 11$ mV in 1 M KOH with a Tafel slope of 31 mV dec^{-1}. It also showed superior hydrogen oxidation activity, with a mass activity of 8.83 A mg^{-1}. Wang *et al.* utilized Pt-rich cores to incorporate strongly repellent element pairs.[76] They fabricated HEA NPs with 14 components. The catalyst delivered $\eta_{10} = 11$ mV in 0.5 M H_2SO_4 and 18 mV in 1 M KOH. It is also a multifunctional electrocatalyst in alkaline media. $E_{1/2} = 0.86$ V for the ORR.

3.5 Critical evaluation of catalytic performance

Most studies evaluate catalytic performance using half-cell metrics. Metrics such as $E_{1/2}$ and overpotential are measured at a current density under 10 mA cm^{-2}. However, device-level performance can deviate from these metrics. They cannot capture catalyst layer utilization, mass transport or membrane/electrolyte compatibility.[77,78] In rechargeable Zn–air batteries, practical evaluation should also include the open-circuit voltage, peak power density, specific capacity and cycling stability.[79] It is important to consider air-cathode degradation, electrolyte instability and Zn-anode failure. Xia *et al.* synthesized bifunctional CoCrCuFeNi/carbon nanofibers (CNFs) for use in rechargeable zinc–air batteries.[80] It delivered an open-circuit voltage of 1.371 V, a peak power density of 87 mW cm^{-2}, a specific capacity of 820 mA h $g_{Zn}{}^{-1}$, and stable operation for 75 h in flexible Zn–air batteries. He *et al.* fabricated FeCoNiMoW NPs.[81] The catalyst showed outstanding performance at both the half-cell and device levels. It achieved an open-circuit voltage of 1.59 V, a peak power density of 116.9 mW cm^{-2}, a specific capacity of 857 mA h $g_{Zn}{}^{-1}$ and stable operation for 660 h. In water splitting applications, CoCrFeMnNi reached 1000 mA cm^{-2} at a low cell voltage (2.18 V) in an anion-exchange-membrane electrolyzer. It remained stable for 200 h at 80 °C in an alkaline environment.[82] Half-cell and device-level performance have different evaluation criteria. An electrochemical device is a system rather than a catalytic material. Practical operation introduces additional mass-transport, interfacial, ohmic, and degradation constraints.[83] Benchmarking at the device level is more complex. The device-level performance is usually less ideal than that implied by half-cell data.

Catalysis occurs at the interfaces. Surface segregation, reconstruction, and dissolution/redeposition processes can alter the surface structure and composition. A controlled dissolution–redeposition equilibrium can be engineered as a stability strategy. *In situ* inductively coupled plasma-optical emission spectroscopy (ICP-OES) measurements of dealloyed HEA electrodes revealed that active elements leach from the surface at the open-circuit potential but are redeposited under cathodic polarization in the acidic HER, maintaining a dynamically changed surface composition rather than progressive degradation.[84] When this dynamic equilibrium was coupled with a protective amorphous oxide overlayer, the net dissolution rates decreased by approximately 80-fold, and stable operation was sustained beyond 2200 h. Recently, single-nanoparticle collision electrochemistry experiments have provided direct statistical evidence that increasing the number of constituent elements from binary to quinary progressively suppresses phase segregation under extreme current densities. Quinary HEA nanoparticles display homogeneous signal distributions comparable to those of monometallic benchmarks, whereas ternary alloys show bimodal responses that are indicative of conductive phase separation.[85] Computationally, machine learning-assisted dissolution simulations across multi-element composition spaces have further shown that alloying with noble metals or elements with high surface energy can result in the formation of protective surface layers. In addition, it can simultaneously drive dissolution pathways toward core–shell structures and provide design guidance for thermodynamically stable HEA catalysts.[86] These findings highlight that identifying the true active state of HEA electrocatalysts requires *operando* tools that can track the near-surface composition, structural evolution, and elemental dissolution simultaneously.

3.6 Trade-off between compositional complexity and catalytic performance

In the past two decades, high-entropy methods have emerged as novel material design strategies. It provides a vast compositional design space and tunable electronic properties. High-entropy can be considered an enabling factor that expands the accessible range of active motifs. However, it should not be considered a necessary approach for better catalytic performance. The relationship between compositional complexity and catalytic performance should be critically revisited.

The performance improvements are sometimes attributed to the specific role of one added element or binary alloys, not from compositional complexity. The bulk composition of HEA electrocatalysts does not necessarily represent the active state during operation. Surface segregation, reconstruction, and

selective dissolution can substantially alter the surface composition and local chemical and electronic environments.[87,88] Various factors can lead to surface compositional changes. Thermodynamically unstable elements dissolve preferentially when in contact with the electrolyte. The surface depletion of certain elements changes the equiatomic configuration.[84] The surface composition during the catalytic process may differ substantially from the design composition. Subsequent electrochemical cycling drives surface reconstruction. The surface structure differs significantly from the bulk structure. Luan *et al.* applied atom probe tomography and TEM to reveal surface and subsurface structural changes.[89] The activated surface of CoCrFeMnNi develops an approximately 5 nm amorphous oxyhydroxide layer enriched in Ni and Fe, while Cr, Co, and Mn are strongly depleted from this outermost region. The reconstructed surface is better described as a binary NiFe oxyhydroxide. A Cr-rich oxide sublayer forms concurrently under this surface layer and temporarily slows the outward migration of the remaining transition metals. Qian *et al.* performed first-principles calculations on CoCrFeMnNi.[26] The adsorption of O* and OH* is highly sensitive to the identity of the local binding atom. It clearly has a preference for Cr-containing sites. Pedersen *et al.* used Bayesian optimization to screen quinary HEA composition spaces for the ORR. After experimental validation, the maximum activity was not quinary. Instead, the best-performing catalysts were binary alloys, including Ag–Pd, Ir–Pt and Pd–Ru.[58]

Theoretically, adding more elements (>5) can broaden the distribution of the adsorption energy and introduce new active motifs. This could be beneficial because of sufficient site diversity. However, diminishing returns can occur. Additional elements may dilute the optimal motif, introduce unfavorable neighbors, or increase segregation and structural complexity.[90] Ye *et al.* conducted a DFT-trained ML algorithm to quickly screen quinary HEA compositions.[91] The composition–activity map revealed that the dominant highly active sites were first-nearest-neighbor triplets composed only of Pt and Pd atoms. The catalytically relevant local motif can remain chemically simpler. The improved performance should not be attributed to the high-entropy effect alone unless lower-order counterparts are compared under the same conditions. Bürgel *et al.* conducted a comparative study on Cu–Pd–Pt–Ru, Ir–Pd–Pt–Ru and Ni–Pd–Pt–Ru systems.[92] The ORR optimum appeared to be located at a strongly Pd-rich composition, $Ir_8Pd_{82}Pt_6Ru_4$, rather than a near-equiatomic composition.

Increasing compositional complexity can also lead to increased synthesis difficulty. With an increasing number of elements, the precursor reduction becomes less synchronized.[93] Bueno *et al.* prepared HEA NPs from core–shell precursors.[94] Intraparticle heterogeneity was observed when Ir or Ru was incorporated. Alloying temperature windows narrow because of different melting points. High compositional complexity can also cause incomplete mixing, short-range ordering, and surface segregation.[95,96] These factors complicate both synthesis and mechanistic interpretation. Moreover, catalytic performance is affected by differences in particle size, morphology, support, metal loading, and testing protocol.[97] It is difficult to isolate the contribution of entropy stabilization to catalytic performance. For this reason, compositional complexity should be treated as a design variable rather than a design target. In some cases, medium-entropy or ternary alloys can indeed provide unique site distributions or improved durability. They can deliver comparable activity with relatively low complexity, better reproducibility and a clearer structure–property relationship.

4. Synthetic methods for HEAs in the ORR/HER

HEA electrocatalysts for the HER and ORR have been produced *via* many routes. The chosen route often sets the phase, the level of disorder, and the surface motifs that appear during operation. Composition is a key design variable. However, synthesis determines whether metals truly mix, which defects form, and when segregation occurs. It also governs how well the as-made structure represents the working catalyst. In this review, the methods are organized into five method classes on the basis of the dominant driving force for alloy formation. Thermal processing enables alloying *via* high-temperature interdiffusion to form robust solid solutions. Flux processing-enabled synthesis supplies a continuous metal flux to access kinetically trapped films or clusters with precise composition control. Redox processing-enabled nucleation and alloying enable scalable routes to nanoscale HEAs, but they depend on synchronized reduction and clean surface chemistry. The electrochemical potential enables alloying to link catalyst formation to electrode architectures, and the surface often continues to evolve under bias. Other enabling methods for alloying and discovery cover precursor–chemistry conversions, external–energy inputs and data-driven high-throughput workflows that accelerate screening and optimization.

4.1 Alloying *via* thermal processing

Thermal processing remains a mainstream route for HEA electrocatalysts since temperature governs phase formation and elemental redistribution. Here, we highlight studies in which heat treatment is the primary driver of alloying. This class includes conventional melt processing, ultrafast Joule or carbon-shock heating, fast-bed moving pyrolysis, melt spinning, and flame synthesis. These methods can yield well-defined compositions and mechanically robust architectures for HER and ORR studies. However, these methodologies often face persistent challenges: (1) coarsening can reduce the active surface area, and (2) surface segregation can distort the intended composition. (3) Mixing can remain incomplete when diffusion rates differ across elements. Overall, thermal routes are reliable and scalable, but they require strategies to suppress sintering and composition drift.

4.1.1 Melt-based metallurgy. Melt-based metallurgy is a direct and well-established route to prepare HEAs. Arc or induction melting followed by homogenization annealing can yield bulk solid solutions with stable phases and reproducible bulk compositions. In HER and ORR studies, these materials often serve as composition benchmarks and robust conductive

backbones. In addition, they can provide prealloyed feedstocks for later powder processing. The main drawback is limited surface exposure. Many studies therefore add atomization, controlled comminution, or selective dealloying to open active sites and tune the near-surface composition. This region largely governs electrocatalysis. Alkraidi *et al.* produced $WMoNbVCr_x$ alloys *via* compact arc melting of pressed powder blends.[98] They evacuated the chamber, purged it with Ar, and remelted each button four times while flipping. This protocol improved mixing but did not eliminate heterogeneity. The alloys still contained W-rich and W-poor regions. This case highlights a common issue in refractory HEAs. Full homogenization can remain difficult even with repeated remelting. Kumari *et al.* used radio frequency induction melting to densify a $Co_{35}Cr_5Fe_{10}Ni_{30}Ti_{20}$ alloy.[99] The pellets were melted in a graphite crucible under Ar flow. The ingot was remelted three to four times with further annealing at 790 °C for 2 h. The resulting phase constitution provided a practical stability check before further thermal processing and revealed how induction melting supports rapid phase validation for later catalyst workflows. Duan *et al.* addressed impurity control when low-cost ferroalloys are used as feedstocks.[100] They melted a CoCrFeMnNi master alloy and refined the melt using $CaO–MgO–Al_2O_3$ slags. A CaO–MgO-saturated slag together with a MgO crucible improved sulfur removal. Sulfur was reduced to the ppm level. This work highlights that melt refining can be as important as alloying itself and that impurities can otherwise mask intrinsic catalytic trends. Shen *et al.* converted TiZrHfNbMo ingots into powders *via* hydrogen-containing plasma, as shown in Fig. 10a.[101] The ingots were treated with 15% H_2/Ar. The collected powders retained a single BCC structure and presented a lower oxygen content than the starting ingot. This

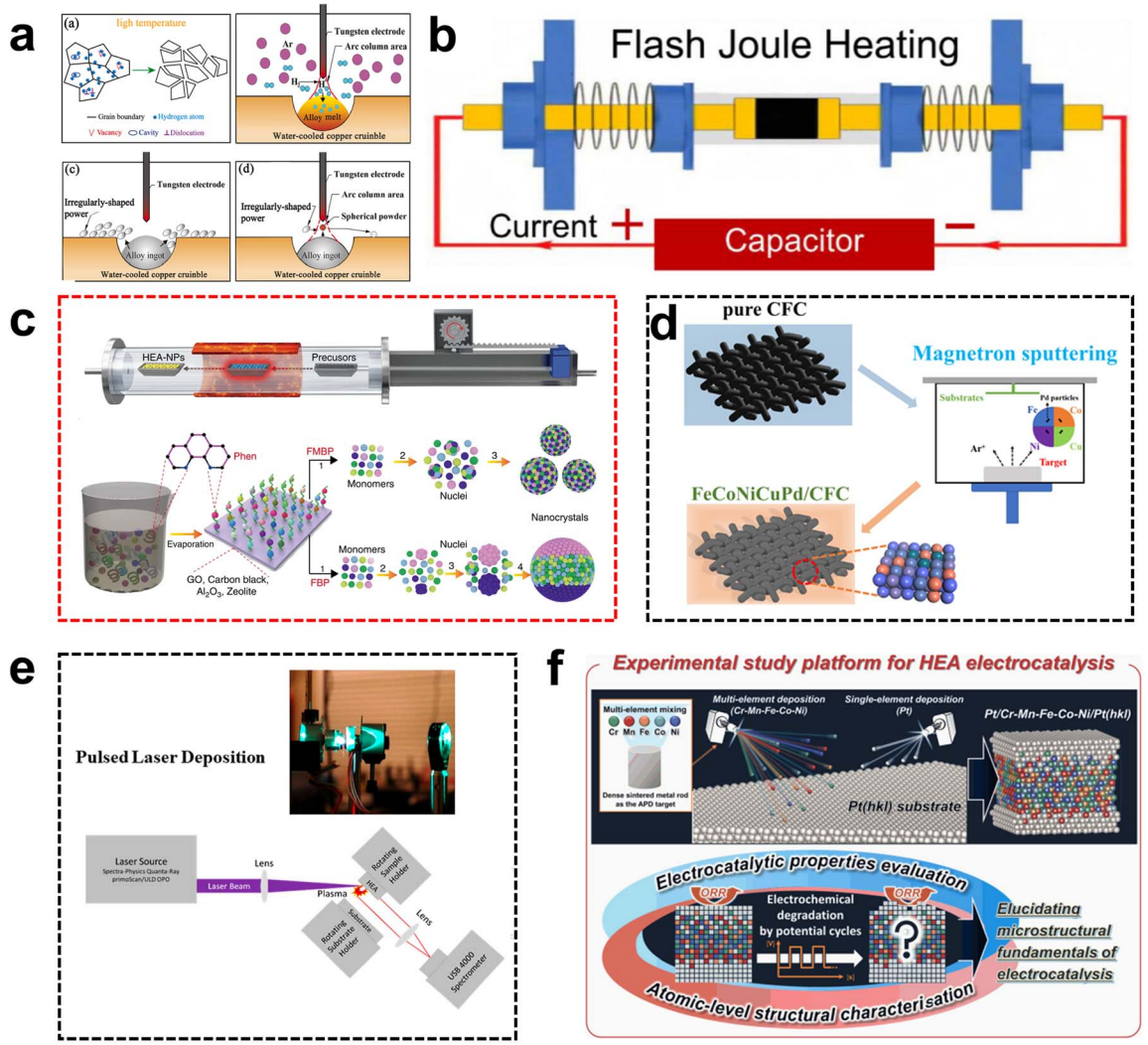

Fig. 10 (a) Schematic diagram of the hydrogen plasma-arc melting method. Reproduced with permission.[101] Copyright 2024, Elsevier. (b) Flash Joule heating device diagram. Reproduced with permission.[102] Copyright 2025, Elsevier. (c) Schematic diagram of the FMBP experimental setup for the synthesis of HEA-NPs. Reproduced with permission.[103] Copyright 2020, Springer Nature. (d) Schematic illustration of key FeCoNiCuPd thin film fabrication steps. Reproduced with permission.[104] Copyright 2022, Elsevier. (e) Schematic illustration of pulsed laser deposition. Reproduced with permission.[105] Copyright 2024, American Chemical Society. (f) Schematic illustration of the experimental study platform of the HEA electrocatalysis model surface *via* multiple arc-plasma depositions. Reproduced with permission.[106] Copyright 2023, Springer Nature.

route connects bulk metallurgy and catalyst processing. It delivers prealloyed powders with controlled compositions.

4.1.2 Ultrafast Joule/carbon-shock heating. Ultrafast Joule heating and carbon thermal shock offer a distinct thermal route for HEA formation. They reach very high peak temperatures within milliseconds with equally rapid cooling. This short thermal history can promote alloying while limiting grain growth, which helps retain small features and high site density. The main risk is nonuniform heating, where temperature gradients and element-specific kinetics can cause local composition drift. Careful control of substrates and pulse conditions is therefore essential. Rigorous postvalidation should accompany these syntheses. In practice, these methods often involve depositing metal salts on carbon supports and applying a single pulse. The pulse drives rapid reduction and interdiffusion. Fast quenching then preserves the mixed state. This timing is useful when metals are reduced at different temperatures. It also reduces the time for coarsening. However, fast processing can conceal incomplete mixing. A consistent phase and mapping workflow is needed to confirm true alloying. Wang *et al.* used shock heating and cooling to form PtFeCoNiMn nanoparticles on ordered mesoporous carbon.[45] Rapid heat pulses promoted alloy formation and suppressed phase separation. *Operando* X-ray diffraction (XRD) was used to track alloying during the pulse sequence. They linked mixed surface motifs to improved ORR behavior. This research shows how ultrafast thermal control can be paired with *operando* validation. Wang *et al.* reported a one-step Joule route to ultrafine αNiCoMn (α = Pt, Ir, and Ru) HEA nanoparticles on N-doped carbon.[107] The precursor combined recovered Ni, Co, and Mn sources with Pt-group salts. Thermal shock enabled fast co-reduction and mixing. The work argued that short shocks reshape the local charge distribution. This was connected to oxygen-related steps in the ORR and OER-type chemistry. This case highlights the sustainability and compositional flexibility of one platform. Li *et al.* used flash Joule heating to form RuVCoCuZnW nanoparticles on carbon nanotubes.[108] The ultrafast pulse created a high-temperature alloying window. Zn loss at high temperatures introduces vacancy-type defects. It also produced a more porous texture. The authors linked these features to enhanced performance at high current in alkaline media and illustrated how shock routes can couple alloying with defect engineering. Huang *et al.* emphasized precursor microenvironment control in carbon thermal shock pyrolysis, as shown in Fig. 10b.[102] They tuned the solvent polarity to reduce ion clustering. They also strengthened particle-support bonding *via* the use of oxidized carbon. These changes keep the particles smaller after the shock step. The catalyst showed improved HER, HOR, and ORR behavior in acid. Wang *et al.* also used carbon thermal shock to prepare FeCoNiMnRuLa on carbon nanotubes (CNTs).[109] La served as a strong size-mismatch element. This increased the degree of lattice distortion and decreased the crystallinity. Overall, ultrafast thermal methods are powerful, but they require tight process control and strong structural proof.

4.1.3 Fast-bed moving pyrolysis. Fast-bed moving pyrolysis provides a continuous and high-throughput thermal route for HEA synthesis. It relies on rapid heat transfer and short residence times to drive precursor conversion and alloying. Compared with batch furnaces, the moving-bed design offers tighter control of the exposure time. It also limits high-temperature dwell, which helps suppress sintering in nanoscale HER and ORR catalysts. Reducing atmospheres or reactive feeds are often used to efficiently reach metallic phases. However, mismatched reduction and diffusion kinetics can still leave secondary phases if conditions are not well balanced. Fast-bed moving pyrolysis usually operates through a rapid thermal jump into a hot zone. The precursor bed enters the hot region within seconds, so mixed salts experience nearly synchronous heating. This feature is important because fixed-bed programs often reduce metals sequentially. Sequential reduction promotes segregation and can accelerate coarsening. In contrast, fast entry into the hot zone creates a brief period of high metal availability. These factors favor burst nucleation and early-stage intermixing before separation becomes pronounced. Overall, the method aims to compress reduction and alloying into a short time window. Gao *et al.* provided a clear demonstration of this concept.[103] They wet-impregnated mixed metal chlorides onto granular supports and processed them by fast-bed moving pyrolysis, as shown in Fig. 10c. The reactor reached approximately 923 K within seconds and maintained a stable hot-zone temperature. Ultrasmall HEA nanoparticles formed on several supports, including graphene oxide, carbon black, γ-Al_2O_3, and zeolite. The approach also extended to higher-order alloys, reaching denary compositions with narrow size distributions near the 2 nm scale. Control experiments clarified the role of the heating speed. A slower moving-bed mode produced phase separation in a model ternary system. Conventional fixed-bed heating led to even stronger separation. Related studies have used fast moving-bed heating to improve dispersion on CNT supports.[110] Rapid heating and cooling yielded smaller and more uniform particles. Slow cooling promoted particle coalescence and broader size distributions. The improved dispersion was then associated with stronger alkaline HER performance. Together, these reports position fast-bed moving pyrolysis as a practical bridge between batch thermal routes and scalable manufacturing, provided that the kinetic balance is maintained.

4.1.4 Melt spinning. Melt spinning produces HEA ribbons by quenching a melt on a rapidly rotating copper wheel. The high cooling rate limits solute partitioning and suppresses composition-rich domains. As a result, ribbons often have refined grains and high grain-boundary density. These features can facilitate later electrochemical activation. However, pristine ribbons still have a limited surface area. Many researchers therefore use them as clean alloy sources and add a second step to increase accessibility. Kumar *et al.* prepared TiZrVCrNi melt-spun ribbons and evaluated their hydrogen uptake.[111] They used RF induction melting under Ar with repeated remelting, followed by wheel quenching into thin ribbons. The XRD results indicated a single C14 Laves phase, and the hydrogen loading capacity reached 2 wt%. The capacity loss over 10 absorption–desorption cycles was small, suggesting good compositional stability after rapid solidification. This work supports the use of

melt spinning as a route to reproduce bulk alloy states. Svalov *et al.* used melt spinning to fabricate GdTbDyHoEr HEA ribbons and tuned the microstructure through wheel speed.[112] Ribbons were produced under Ar at 10–40 m s^{-1}. The samples retained a single hexagonal structure consistent with that of the bulk alloy. The ribbon form improved the magnetocaloric response relative to that of the ingot. The processing speed alters the microstructure, and the microstructure shifts the functional response. Ma *et al.* extended rapid solidification to a fiber geometry *via* an in-rotating-water spinning method.[113] They produced long HEA fibers with diameters near 180 μm. The fibers combine strength with flexibility, which enables self-supporting architectures. Annealing reduced coercivity while largely preserving magnetization. Such formats can be useful when a robust metallic scaffold is needed before surface opening steps.

4.1.5 Flame synthesis. Flame synthesis uses combustion heat to drive rapid precursor conversion and multimetal mixing. Metal precursors are blended into a fuel and burned in air. The flame creates a high-temperature reaction zone with steep gradients. A nearby collector captures soot-like carbon nanoparticles that host the metal species. This route is continuous and does not require a furnace or vacuum. This approach is therefore attractive for fast, scalable catalyst preparation. Liu *et al.* demonstrated a simple flame route to multimetal catalysts supported on soot.[114] They dissolved metal acetylacetonates in paraffin wax and used a candle flame as the heat source. The flame behaved like a flow reactor. The precursors passed through the hot zone, decomposed, and then condensed onto the soot generated in the same flame. The collected soot contained onion-like carbon particles decorated with metal species. Product speciation depends on the degree of metal loading. A higher precursor feed shifted the output from isolated sites to nanoparticles. The method also tolerates wide composition choices and maps confirmed mixed distributions in selected samples. Overall, flame synthesis is rapid and simple, but controlling its composition requires careful precursor management.

4.2 Flux processing-enabled synthesis

Flux processing results in the formation of HEA catalysts by the delivery of metal atoms or clusters onto a substrate. The incident flux governs intermixing and determines the effective growth rate. This provides direct control over the composition and enables kinetically trapped mixed states. Such states can be difficult to preserve by postannealing. These routes commonly produce thin films or supported nanoparticles for the HER and ORR. The products often function as clean model electrodes with well-defined chemistries. They also enable rapid composition screening across multimetal spaces. A practical limitation is low mass loading. Several studies therefore use porous supports or roughened substrates to increase the accessible site density. Overall, flux processing is powerful for controlled synthesis and screening, but scaling and site density need deliberate design.

4.2.1 Magnetron sputtering. Magnetron cosputtering is a widely used route for preparing HEA thin films. It employs two or more targets, and the target power directly affects the film composition. Many groups also use composition spreads, thus, one wafer spans a broad library. Process variables such as pressure, substrate temperature, and bias further alter the density, stress, and texture. The resulting films adhere well to conductive supports, which are suitable for HER and ORR testing. However, films typically have a small surface area, and the surface composition can deviate from that of the bulk. Postannealing can improve intermixing, but it often increases the grain size. Overall, sputtering offers precise control and clean electrodes, but surface accessibility remains a constraint. Wang *et al.* deposited a FeCoNiCuPd HEA film on carbon fiber cloth by pulsed direct current (DC) magnetron sputtering, as shown in Fig. 10d.[104] The process uses multiple metal targets under Ar at low working pressures. The film appeared smooth and continuous, with a single FCC phase and uniform elemental maps. The film served directly as a binder-free electrode for alkaline water splitting. The HER activity was attributed to multiple surface motifs, while the OER activity involved an oxyhydroxide layer formed during operation. Schwarz *et al.* used DC magnetron sputtering to grow CoCrFeNi films on MgO(100).[115] They obtained single-crystalline, well-oriented films with near-equimolar compositions. The elemental maps revealed no obvious segregation. The authors treated these films as model HEA surfaces and examined their composition and surface order *via* surface-sensitive methods. This work is important for catalysis because it demonstrates a clean platform for structure–property analysis without binders or additives. Li *et al.* prepared FeNiMoCrAl and related alloy films on Ni foam by cosputtering and evaluated the OER.[116] The coating had a uniform thickness and a mixed metal distribution. The as-deposited film was amorphous, and surface evolution was tracked under OER conditions. A comparison of the unary and quinary compositions revealed that the multimetal film was the best performer with strong stability. Tight film–support contact helps maintain fast charge transfer during gas evolution.

4.2.2 Pulsed laser deposition. Pulsed laser deposition (PLD) growth is frequently kinetically governed because the plume arrives at short bursts. The laser fluence, repetition rate, background gas, and substrate temperature affect the texture and phase selection. This makes PLD suitable for rapid screening of the composition–structure space. Moreover, near-surface artifacts can bias HER and ORR readouts. A consistent protocol for surface morphology, composition depth profiles, and oxidation states helps maintain interpretability. Overall, PLD offers flexible composition control, but careful validation of the catalytic surface is needed. Lu *et al.* deposited $CoCrFeNiAl_{0.3}$ films on Si at room temperature under high vacuum.[117] The films contained nanoscale surface granules, and the deposition time affected the hardness and modulus. The study also reported improved corrosion resistance in NaCl compared with 316L stainless steel, thus suggesting PLD as a route to compact multimetal coatings with tunable microstructures. Mahdavi *et al.* performed PLD in open air at

atmospheric pressure and deposited AlCrFeMnTi on fluorine-doped tin oxide (FTO), as shown in Fig. 10e.[105] They examined how the laser wavelength influences the phase constitution, microstructure, and corrosion response. The open-air setup decreases hardware demands, but it increases sensitivity to oxygen-driven surface chemistry. This is a key point when the target application is electrocatalysis. Miyajima *et al.* introduced a rotating segmented target to avoid prefabricating a bulk HEA target.[118] Their target used pure Cr, Mn, Fe, Co, and Ni sectors and produced Cantor-like films on glass, aluminum, and steel. The film thickness depended on the chamber pressure and substrate choice, and the coatings acted as oxygen-permeable barriers.

4.2.3 Arc-plasma deposition. Arc-plasma deposition (APD) generates a metal flux by striking an arc on a target under high vacuum. The flux is deposited onto single-crystal substrates and forms thin alloy layers. Growth occurs under clean conditions, so the surface composition is well controlled. APD also enables sequential stacking and postannealing to tune intermixing. This makes it valuable for mechanistic ORR studies that require defined surfaces. Its main limitation is scale, so it is primarily a model-surface tool rather than a bulk synthesis route. Chida *et al.* developed an integrated platform that couples APD growth with electrochemistry without air exposure.[106] Fig. 10f shows the experimental study platform of the HEA electrocatalysis model surface *via* multiple arc-plasma depositions. The system used multiple APD sources in an ultrahigh-vacuum chamber. They deposited Pt and an equiatomic Cr–Mn–Fe–Co–Ni layer onto Pt (*hkl*) single crystals. Layer thickness was monitored by a quartz crystal microbalance, followed by annealing to promote near-surface mixing and stabilization. The sample was then transferred to a N_2 electrochemical setup without air contact. This avoided premature oxidation of less noble elements. This workflow enables cleaner structure–activity correlations than *ex situ* transfer does. Overall, APD provides a controlled route to stable, composition-engineered ORR model surfaces.

4.3 Redox processing-enabled nucleation and alloying

Redox processing is a direct route to HEA catalysts because reduction converts ions or oxidized precursors into zero-valent atoms and initiates nucleation. The reduction pathway determines when each element appears and how fast the particles grow. It also determines whether a single mixed alloy forms or separates into element-rich domains. These kinetic choices therefore shape the final phase and surface chemistry. In the HER and ORR literature, two redox routes dominate. Solution coreduction offers straightforward access to supported nanoparticles, but it requires tight control of reduction synchrony and residual surface species. Gas–solid reduction can process oxides or salts at scale, but it must suppress sintering and manage element-dependent reduction rates. The next sections compare these two routes and highlight their practical trade-offs.

4.3.1 Solution coreduction. Liquid-phase coreduction results in the formation of HEA nanoparticles when multiple metal precursors are reduced in one solution. Metals have different redox potentials, so their reduction rates rarely match. Successful recipes compress nucleation into a short window using strong reductants and coordinating ligands. This route runs at moderate temperature and supports direct deposition on carbon. It also enables size and shape control. The main risk is segregation, thus, reducing synchrony and growth control are critical. Yu *et al.* synthesized PtPdFeCoNi HEA nanoparticles *via* high-temperature injection.[119] Rapid injection promoted burst nucleation and reduced early-stage segregation. The particles behaved as solid-solution alloys and showed strong ORR activity with improved durability. The authors attributed the stability to lattice distortion and sluggish diffusion, which can suppress coalescence and leaching during cycling. He *et al.* reported a low-temperature solution route to FeCoNiMoW HEA nanoparticles, as shown in Fig. 11a.[81] Structural analysis indicated a well-mixed alloy with small lattice distortions rather than phase-separated domains. The material acted as a bifunctional oxygen catalyst, and the performance was linked to Mo/W-driven electronic tuning. DFT suggested a shifted d-band center that optimizes the adsorption of key oxygen intermediates, which supports both activity and stability during zinc–air operation. Wang *et al.* developed a one-pot route to Ru-doped PtFeNiCuW HEA octahedra on CNTs.[50] Ru dopants and $W(CO)_6$ promoted the concurrent reduction of multiple precursors and improved size uniformity. The calculations suggested site differentiation, where W-rich sites assist water activation and nearby Cu-based hollow sites facilitate H* release. Chen *et al.* used solvent reduction to form convex-cube $Pt_{34}Fe_5Ni_{20}Cu_{31}$-$Mo_9Ru$ nanocrystals on CNTs.[51] They proposed that Ru steers growth and drives facet evolution toward high-index surface features. This morphology route increases the exposure of reactive motifs without the need for vacuum deposition. In summary, these studies demonstrate that liquid coreduction can achieve both compositional mixing and morphology engineering, provided that the reduction kinetics are controlled.

4.3.2 Gas–solid reduction. Gas–solid reduction forms HEAs by annealing mixed precursors in a reducing atmosphere, typically H_2/Ar. The gas removes anions and converts salts or oxides into metals, whereas diffusion and coalescence drive alloying toward a single phase. The setup is simple and scalable because it relies on tube furnaces and solid powders or coated supports. It also avoids surfactants, which simplifies surface cleaning. Gas switching provides additional functionality, including NH_3 nitridation or posttreatment. The main challenge is sintering, so support and heating ramps require careful design. Overall, this route balances practicality with strong sensitivity to thermal history. Zhao *et al.* prepared PtCoFeNiCu HEA nanoparticles on Vulcan carbon by drying mixed precursors and annealing them under flowing H_2/Ar.[126] A second NH_3 anneal introduced nitrogen, and acid washing yielded a Pt-rich skin on an N-doped HEA core. *In situ* synchrotron XRD resolved three stages: early reduction, emergence of an FCC Pt phase, and progressive peak shifts as other metals diffuse into Pt. Chen *et al.* followed a related strategy and extended it beyond noble systems.[127] They formed homogeneous salt mixtures, removed the solvent to form a slurry, and annealed it under 5% H_2/Ar to obtain multicomponent HEAs. The temperature variation clarified the conversion window. Lower temperatures resulted in

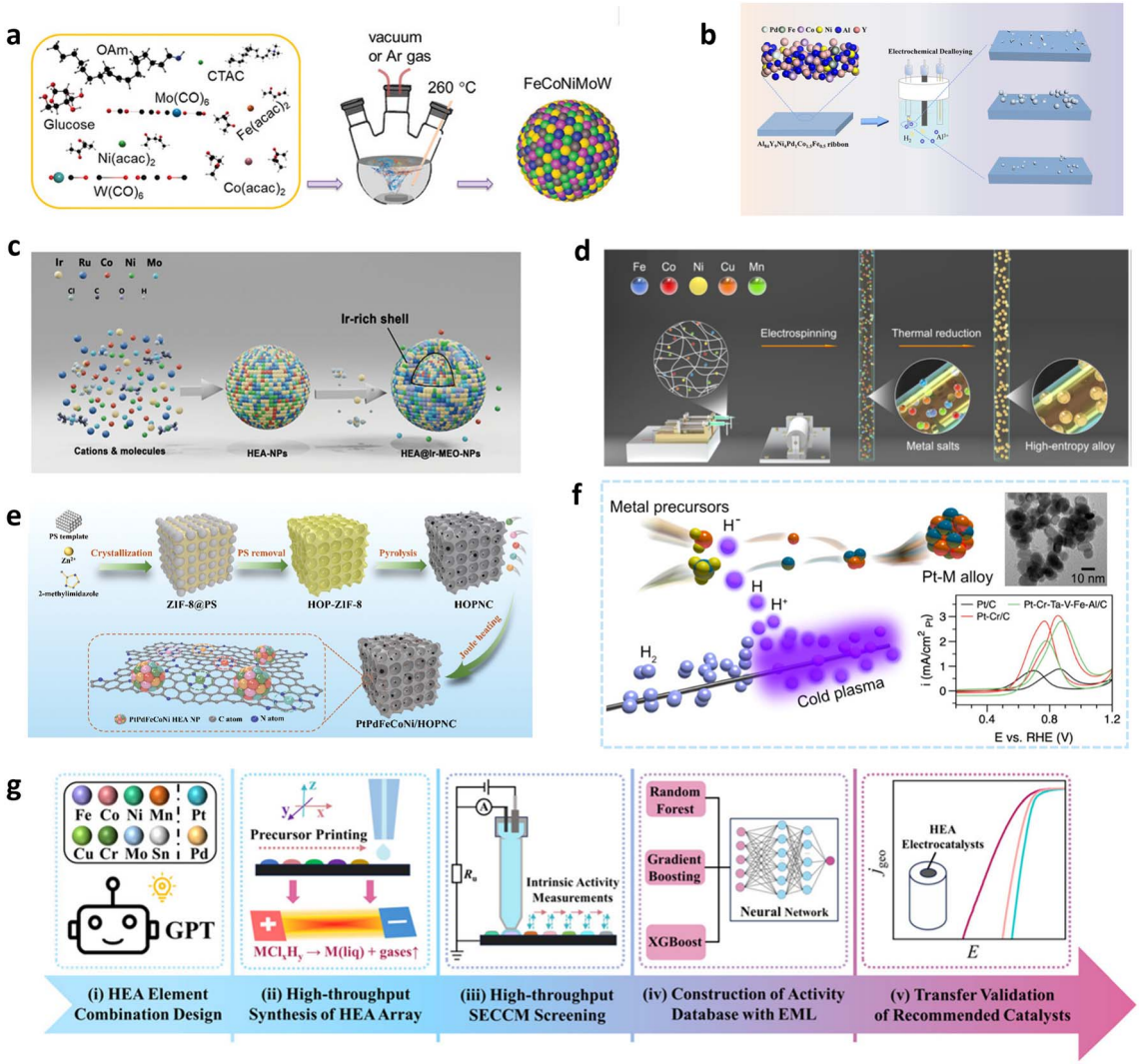

Fig. 11 (a) Schematic diagram of the colloidal synthesis process used to produce FeCoNiMoW nanoparticles. Reproduced with permission.[81] Copyright 2023, Wiley-VCH GmbH. (b) Schematic of the preparation of the Ni–Pd–Co–Fe catalyst. Reproduced with permission.[120] Copyright 2025, Royal Society of Chemistry. (c) Schematic of the prepared HEA and HEA@Ir-MEO. Reproduced with permission.[121] Copyright 2024, Wiley-VCH GmbH. (d) Synthesis procedure of HEA/CNF hybrid nanomaterials through a polymer fiber nanoreactor. Reproduced with permission.[122] Copyright 2023, Royal Society of Chemistry. (e) Schematic illustration of the preparation of PtPdFeCoNi/HOPNC. Reproduced with permission.[123] Copyright 2025, Wiley-VCH GmbH. (f) Schematic illustration of the hydrogen cold plasma synthesis of Pt-RMA and Pt-HEA nanoparticles, with the inset figure showing a DBD reactor. Reproduced with permission.[124] Copyright 2022, American Chemical Society. (g) Workflow for accelerating the discovery of efficient HEA electrocatalysts by combining high-throughput experimentation with data-driven strategies. Reproduced with permission.[125] Copyright 2024, American Chemical Society.

incomplete reduction or residual secondary phases, whereas higher temperatures improved alloying and modified the lattice strain. Bollu *et al.* demonstrated a self-supported electrode design based on stepwise gas–solid processing.[128] They first reduced Co–Ni hydroxide nanowires on Ni foam into Co–Ni alloy nanowires under Ar/H_2. They then introduced additional elements and formed CoNiFeZrPt HEA nanoparticles *via* high-temperature chemical vapor deposition (CVD) tube treatment at 5% (H_2 + Ar). The first step created a conductive backbone, whereas the second step enabled slower multielement diffusion and final alloying. This further shows how gas–solid reduction can build both architecture and composition in one sequence.

4.4 Alloying enabled by electrochemical potential

Electrochemical methods use applied potential to drive deposition, selective dissolution, and surface exchange. The voltage or current is the primary control, unlike thermal routes, which rely on temperature. Alloying can therefore occur locally at the electrode surface and often at low temperatures. This enables direct growth on conductive supports with intimate contact and efficient charge transport. It also supports modular sequences, such as deposition followed by dealloying to create porosity or galvanic replacement to form a skin or add a second metal. The main challenge is kinetic mismatch. Different metals respond differently to the same potential, which can introduce

composition gradients and phase separation. An effective process design is therefore needed to maintain uniform mixing.

4.4.1 Electrodeposition. Electrodeposition results in the formation of multimetal films or supported nanoparticles by reducing metal ions on a conductive substrate. Deposition can be driven by constant potential, constant current, or pulsed waveforms. The approach is fast and scalable, and it avoids high-temperature furnaces. The composition is set mainly by bath chemistry and the electrical program.[129] The key variables include the ion ratio, complexing agent, pH, and pulse parameters. Pulse plating is often helpful because it separates nucleation from growth and improves mixing. The central challenge is reducing potential mismatches across metals. Noble ions deposit earlier, whereas fewer noble ions lag behind. This can generate layered structures or composition gradients. Common mitigation strategies include stronger ligands to narrow effective potential gaps and higher overpotentials to promote coreduction. Improved mass transport, such as stirring, rotation, or flow cells, is also important. Many HEA deposits start being amorphous or nanocrystalline, and electrochemical cycling can further homogenize the near-surface region through dissolution and redeposition. Overall, electrodeposition offers strong controllability, but uniform codeposition must be engineered. Fu *et al.* used soft-template electrodeposition to create a mesoporous PtPdRhRuCu HEA film.[130] The template promoted uniform nucleation and steady growth and was then removed after deposition. The film retained ordered mesopores and presented a single-phase alloy signal. Elemental maps and line scans confirmed the uniform composition across the thickness. These findings also show that the film thickness is easy to tune by the deposition time, whereas the pore structure remains stable. Aliyu and Srivastava electrodeposited AlFeCoNiCu coatings on mild steel and added graphene oxide to the bath.[131] Increasing the amount of graphene oxide (GO) made the coating finer and more compact. XRD indicated mixed BCC and FCC phases, with a higher FCC fraction at higher GO contents. Electrochemical tests revealed reduced corrosion rates as the amount of GO increased. TEM images revealed an Al-rich matrix with dendritic Co–Ni–Cu–Fe regions, and GO improved the compositional uniformity. Percival *et al.* used electrodeposition to access compositions through an oxide intermediate.[132] They deposited an amorphous five-element high-entropy oxide from a nanodroplet emulsion containing mixed salts. Subsequent thermal treatment converted the particles into crystalline FeNiCo alloy nanoparticles with a separate $CrMnO_x$ cophase. Electrodeposition can access multimetal precursors that are difficult to form *via* standard solution routes. Growth at the electrode also enables the formation of ligand-free products. Jo *et al.* combined electrodeposition with a short tellurization step to form a high-entropy chalcogenide.[133] They first codeposited Co, Fe, Ni, Mo, and W onto carbon paper. They then introduced Te to form CoFeNiMoWTe. The final material had an amorphous porous nanosheet architecture. This two-step scheme separates metal mixing from nonmetal incorporation, which simplifies process control.

4.4.2 Electrochemical dealloying. Electrochemical dealloying converts a prealloyed precursor into a porous, catalytically active surface. A controlled potential window selectively dissolves the more reactive elements. The remaining atoms then reorganize and form a nanoporous network or a noble-enriched skin. This transformation increases the surface area and exposes low-coordination motifs. It also introduces strain, which can enhance catalytic kinetics. This method often yields binder-free electrodes with good electrical connectivity. Dealloying outcomes are primarily set by potential, time, and electrolyte. Mild conditions preserve mechanical integrity and enable partial dealloying. Aggressive conditions can over-etch the framework and trigger cracking or collapse. Compositional drift is another recurring issue since continued leaching enriches noble elements at the surface. As a result, peak performance often occurs at an intermediate degree of dealloying rather than at maximum removal. Brief annealing or gentle cycling is typically used to stabilize ligaments and retain the tuned surface state. Chen *et al.* dealloyed a bulk FeCoNiAlMo HEA that contains FCC and BCC phases in a choline chloride-ethylene glycol deep eutectic solvent.[134] The Al-rich FCC phase dissolved preferentially, whereas the Mo-rich BCC phase resisted corrosion and supported the framework. By tuning the potential and time, they obtained a uniform 3D porous surface without obvious cracking. The porous surface improved the charge transfer and enhanced the alkaline OER performance. Li *et al.* used $Al_{84}Y_9Ni_4Pd_1Co_{1.5}Fe_{0.5}$ ribbons and selectively removed Al by electrochemical dealloying, as shown in Fig. 11b.[120] The surface evolved into a self-supported nanosheet–nanosphere architecture enriched with the remaining metals. The reconstructed electrode showed a low OER overpotential in alkaline electrolyte and remained stable for tens of hours. The authors linked the gains to increased accessible sites, defect-rich features, and multimetal synergy within a disordered matrix. Abid *et al.* used Cu as a sacrificial element in a Cantor-type CoCrFeNiMn alloy.[135] Limited Cu solubility caused interdendritic segregation during solidification. Subsequent electrochemical dealloying in dilute nitric acid removed Cu and increased the interconnected micrometer-scale porosity. The dense alloy was converted into a foam-like architecture with improved electrochemical storage behavior, largely due to its greater internal surface area and easier transport.

4.4.3 Electrochemical galvanic replacement. Electrochemical galvanic replacement deposits a noble metal onto a less noble surface through coupled reduction and dissolution. Noble metal ions are reduced at the surface, while the host metal partially dissolves. The applied potential can slow or accelerate this exchange and improve uniformity. This method is useful for core–shell particles, noble-metal skins, hollow structures, and surface doping layers. It modifies the near-surface region without fully remaking the bulk alloy. Yao *et al.* reported sub-2-nm IrRuCoNiMo HEA nanoparticles with an Ir-rich medium-entropy oxide shell, as shown in Fig. 11c.[121] They first formed an HEA core *via* rapid solution reduction. An Ir precursor was then introduced for a galvanic replacement step. The surface Co, Ni, and Mo provided electrons for Ir deposition, enriching Ir near the surface. Depth profiling supported a few-layer Ir-rich oxide shell. The shell protected less noble elements during the acidic OER, reducing dissolution and slowing structural drift. The authors attributed this activity to the more favorable formation of key

OER intermediates on the modified Ir-oxide surface. Tao *et al.* used a template-based galvanic exchange route to obtain ultrathin HEA ribbons.[136] They started from Ag nanowires and introduced mixed metal precursors. Galvanic exchange replaced surface Ag atoms with more noble metals, and then coreduction filled the shell with additional metals. Subsequent dealloying removed the Ag core, and the shell collapsed into a ribbon-like alloy. Elemental maps indicated a uniform metal distribution along the ribbon. Once a mixed shell forms, the later steps can lock in the alloy and remove the template.

4.4.4 Electrospinning. Electrospinning provides a fiber-confined route to multimetal catalysts. A high electric field draws a polymer solution into continuous fibers. Metal salts or nanoreactors can be codissolved, which distributes metals along the fiber length. Subsequent heat treatment converts the polymer and triggers phase formation. Calcination can generate oxide fibers, whereas reductive annealing can yield multimetal alloys. The products are often free-standing mats with open transport pathways, enabling binder-free electrodes. The fiber diameter is tunable through the voltage, flow rate, and solution viscosity. Zhu *et al.* synthesized FeCoNiCuMn HEA nanoparticles *via* a polymer fiber nanoreactor strategy, as shown in Fig. 11d.[122] Five metal salts were dissolved in polyacrylonitrile (PAN)/*N*,*N*-dimethylformamide (DMF) and electrospun into a nanofibrous membrane. Stabilization induced PAN cyclization and initiated precursor decomposition. High-temperature treatment then drove nucleation and alloying within the PAN-derived carbon nanofibers, yielding HEA@CNF architectures. Microscopy and elemental mapping revealed uniform mixing without obvious phase separation, which is consistent with an FCC-type HEA. The self-supported membrane served directly as an electrode for the alkaline HER and OER. The authors linked activity to site-level electronic tuning driven by electronegativity differences. Cai *et al.* combined metal–organic framework (MOF) confinement with electrospun fibers to control HEA size.[72] They first loaded Pt, Ru, Pd, Co, and Ni ions into ZIF-8 nanoparticles and then electrospun ZIF-8 into the PAN fibers. Calcination carbonized PAN and collapsed ZIF-8, producing porous carbon fibers with embedded PtRuPdCoNi HEA nanoparticles. The particle size was tuned by adjusting the metal loading in ZIF-8, which reduced aggregation during conversion. The product formed a flexible, porous membrane with uniformly distributed ultrasmall HEA nanoparticles. The platform was used to probe size effects on the HER and ORR and was consistent with DFT-guided trends.

4.5 Other enabling methods for alloying and discovery

Other enabling methods can form HEAs without relying on furnace annealing or conventional solution coreduction as the primary driver. These approaches use precursor chemistry to preorganize metals, external energy inputs to accelerate mixing, or data-driven screening to reduce trial and error. They often shorten the synthesis time and improve compositional uniformity. They can also generate porous architectures and defect-rich surfaces that are difficult to access by slow heating. However, process control is often less intuitive, and viable parameter windows can be narrow. Strong evidence for phase identity and compositional homogeneity therefore remains essential.

4.5.1 Precursor chemistry-enabled assembly and conversion. Precursor-chemistry routes use molecular design to control mixing before alloying begins. Multiple metals are first integrated into a shared precursor, such as a framework or a gel network. A subsequent conversion step then produces the target phase. The main advantage is ion-scale mixing in the precursor. This reduces segregation during conversion and improves compositional uniformity in the final catalyst. Overall, the precursor acts as a blueprint for both composition and local structure.

(1) MOF-derived conversion

MOF-derived conversion uses an MOF as both a metal reservoir and a nanoreactor. Metal ions can be incorporated into the framework at defined ratios. During thermal conversion, organic linkers carbonize into N-doped carbon, while metal nodes or guest ions reduce into alloy nanoparticles. The rigid scaffold constrains atomic migration, which promotes phase mixing and suppresses particle coarsening. As a result, MOF-derived routes often yield uniform dispersion and strong metal–support coupling, which benefits electrocatalytic stability. Qiu *et al.* developed a 2D MOF-assisted pyrolysis-replacement-alloying strategy to prepare CoCuFeAgRu HEA nanoparticles on porous N-doped carbon nanosheets.[137] The precursor nanosheet morphology was largely retained after conversion, and the HEA nanoparticles remained uniformly distributed on the ultrathin carbon. Structural characterization supported an FCC alloy with a broadly homogeneous elemental distribution. The authors proposed functional differentiation within the multimetal composition, with Ag favoring the ORR and Ru favoring the OER, while Co, Cu, and Fe increased the entropy and tuned the electronic structure. The catalyst showed durable bifunctional oxygen electrocatalysis and was demonstrated in Zn–air batteries, including stable operation at very low temperatures. Xie *et al.* emphasized MOF-derived porous carbon as a spatial cage for multimetal sites, as shown in Fig. 11e.[123] They prepared hierarchically ordered porous ZIF-8 *via* a template and then carbonized it into a 3D N-doped carbon framework. Metal ions were absorbed into this scaffold and converted by rapid heating into PtPdFeCoNi HEA nanoparticles, together with dispersed single atoms. The open pore network improved mass transfer, whereas N sites anchored metal species and suppressed sintering. Thus, MOF-derived conversion can integrate composition control, confinement, and transport design within one synthesis sequence.

(2) Sol–gel-assisted conversion

Sol–gel-assisted conversion uses solution chemistry to premix metals before alloying. Multiple precursors are first codissolved and then immobilized within a gel network. This gel step helps preserve target ratios and suppresses early segregation. After drying, a short thermal treatment converts the gel into an alloy or into an oxide that can be further reduced or dealloyed. Key controls include chelation strength, pH, and removal of organics. Poor control can leave residual carbon or oxide and can shift the composition. Li *et al.* prepared

a ZnFeNiCoCr HEA *via* a nitrate-based sol–gel route with citric acid chelation.[138] Citric acid coordinated the five metals and formed a cross-linked gel that maintained close contact. The dried gel was annealed under N_2, with excess Zn added as a sacrificial component. At high temperatures, Zn was preferentially removed, creating a nanoporous structure, while the remaining metals formed a single-phase alloy. The elemental maps supported uniform mixing, which was consistent with effective gel-level homogenization. Niu *et al.* demonstrated sol–gel autocombustion as a rapid route to nanocrystalline HEAs.[139] They used metal nitrates as oxidants and citric acid as both a fuel and a coordinating agent. The sol was neutralized, dried into gels at 90 °C, and ignited at approximately 300 °C. Gas analysis indicated that combustion produced reducing species that enabled *in situ* reduction during conversion. The phase outcome depended strongly on the fuel-to-oxidant ratio, with ratios near unity yielding solid-solution features with FCC and BCC characteristics. Postannealing further reduced residual oxide signatures.

4.5.2 External-energy-enabled synthesis and activation. External-energy-assisted routes use nonthermal inputs to drive rapid reactions or localized heating. Their primary aim is to shorten the diffusion time and limit phase separation during alloying. Because the energy input is brief and spatially concentrated, these methods often access nonequilibrium states. They can also introduce defects and lattice strain that are difficult to obtain under slow furnace annealing.

(1) Laser-assisted synthesis

Laser-assisted synthesis uses a focused beam to deliver energy into a confined region. Heating and cooling both occur rapidly, which compresses the thermal exposure time. This short thermal history can promote multimetal mixing before long-range diffusion and segregation develop. Laser processing can also locally restructure surfaces, creating new motifs without changing the entire bulk. These features support two common uses in HEA catalysis. One is to convert salt coatings into HEA nanoparticles. The other method involves reconstructing premade alloys into more active electrodes. The key controls include the laser power and dwell time, as well as the surrounding atmosphere or solvent. Li *et al.* reported a rapid approach based on a continuous-wave visible laser.[140] The mixed metal salts were drop-cast onto porous carbon nanofibers or glass. Millisecond irradiation converted the coating into crystalline HEA nanoparticles. The irradiation time tuned the outcome, shifting the products from single-phase HEAs to multiphase HEAs. Spatially resolved XRD was used to track the phase evolution along the laser path. Liu *et al.* applied laser processing as a surface reconstruction tool for a bulk HEA.[141] They designed a NiFeCrVTi composite *via* high-throughput computation and prepared it by melting and powder metallurgy. Laser etching at different powers generated ordered textures and increased porosity. It also removed the Ni_3Ti secondary phase in an optimized sample. Park *et al.* used pulsed laser irradiation in liquids to deposit RuPdIrPtAu HEA nanoparticles on CNTs.[142] Metal salts were first adsorbed onto the CNT surfaces and then reduced under laser pulses in the liquid phase. The resulting particles were small and uniformly distributed, and the irradiation time was used to tune the loading and structure. No-laser control did not yield the desired HEA, confirming that laser input drives reduction and alloying *via* this route.

(2) Ultrasound-assisted synthesis

Ultrasound-assisted synthesis uses acoustic energy to accelerate multimetal reduction and assembly in liquids. Acoustic cavitation generates transient high-energy microenvironments, whereas the bulk remains near ambient temperature. This can compress nucleation into a short time window and promote early-stage mixing. It is therefore useful for HEAs where coreduction is otherwise asynchronous. Ultrasound also improves dispersion and interfacial contact, which aids anchoring on carbons and 2D supports. The outcomes depend on the reactor geometry, probe position, and delivered power, so these parameters should be reported clearly. Liu *et al.* developed an ultrasonication-assisted polyol route to PtAuPdRhRu HEA NPs.[143] Equimolar amounts of noble metal precursors were dissolved in ethylene glycol with XC-72 carbon as the support. Probe ultrasonication under ambient conditions triggered rapid coreduction and particle formation. The as-prepared product was amorphous and carbon-supported, and N_2 calcination promoted alloy maturation. After annealing, the material exhibited a single FCC phase with a uniform elemental distribution. Urs *et al.* used sonochemistry to assemble HEA-2D hybrid junctions.[144] Ag–Au–Cu–Pd–Pt HEA nanoparticles were prepared first and then mixed with cryomilled MoS_2 in water/DMF. Extended ultrasonication exfoliated MoS_2 and promoted uniform nanoparticle decoration on the nanosheets. The resulting HEA-MoS_2 junction showed electronic changes and improved hydrogen sensing.

(3) Microwave-assisted synthesis

Microwave-assisted synthesis uses electromagnetic radiation to heat reactive media quickly. Heating can be volumetric, so the whole sample warms at once rather than from the outside in. This can shorten the time needed for reduction and alloying. It can also narrow the window for phase separation. In many HEA systems, the benefit is simple. Faster heating results in faster nucleation and less time for atoms to segregate. This method is used in liquids to make ultrasmall nanoparticles. It is also used in solids to form dense coatings with strong bonding. Zhao *et al.* reported rapid microwave radiation to synthesize sub 2 nm PtRuMoFeCoNi HEA quantum dots.[145] They used a microwave polyol route at elevated temperature for a short time. The microwave input rapidly decomposed acetylacetonate salts and triggered explosive nucleation in triethylene glycol. The solvent also acted as a surface stabilizer and limited growth. HAADF-STEM and elemental mapping revealed uniform mixing within individual dots. XRD revealed broad alloy features that matched the ultrasmall size and lattice distortion. It increases atom utilization by decreasing the size. It also improves mixing in a system with very different reduction tendencies. Nair *et al.* used a microwave route to construct Al_xCoCrFeNi HEA coatings on stainless steel 316L.[146] They spread premixed elemental powders on a substrate and used a 2.45 GHz microwave system with a susceptor to initiate heating. Once coupling starts, the volumetric heating of the powder accelerates melting and

mixing. The cross sections revealed a diffuse interface without a sharp boundary, which supported metallurgical bonding. The coating microstructure evolved with increasing Al content. The phase trend shifted from FCC to BCC as the amount of Al increased. They also observed secondary phases and discussed the role of element diffusion from the substrate. This example highlights the practical value of microwave processing for coatings. It reduces the process time and results in strong adhesion. It also enables composition-dependent phase tuning in one platform.

(4) Plasma-assisted synthesis

Plasma-assisted synthesis uses ionized gases to generate reactive species that drive reduction and alloying. Its main advantage is high chemical reactivity at mild bulk temperatures. This is helpful when metals have widely separated reduction potentials. It also benefits oxyphilic elements that oxidize readily under conventional processing. Plasma exposure can compress the reduction window and promote near-synchronous nucleation. By shortening the time for segregation, plasma routes can improve alloy formation. Wu *et al.* developed an ambient hydrogen cold-plasma method to synthesize Pt-reactive metal alloys and a Pt-based HEA, as shown in Fig. 11f.[124] They used a dielectric barrier discharge reactor to generate H_2 cold plasma at room temperature and atmospheric pressure. The method produced several Pt-M alloys, including Pt–Cr, Pt–Ta, Pt–V, Pt–Fe, and Pt–Al, and it was extended to a secondary Pt–Cr–Ta–V–Fe–Al HEA. The reduction was completed within minutes. The XRD peak shifted relative to that of the Pt-supported alloy. X-Ray photoelectron spectroscopy (XPS) and EDS mapping indicated the presence of mixed metallic elements within the particles.

(5) Mechanochemical synthesis

Mechanochemical synthesis uses mechanical energy to promote alloying without a high-temperature furnace step. Repeated high-energy impacts fracture and cold-weld powders, renewing interfacial contact and shortening diffusion distances. This can enable HEA formation under milder thermal budgets than many rapid heating routes can. Ball milling is also scalable and can be performed in a solvent-free manner. The key process variables include the milling time, rotation speed, ball material, ball-to-powder ratio, atmosphere, and process control agents that limit excessive cold welding. Lu *et al.* reported a solvent-free ball-milling strategy in which graphite served as an interlayer nanoreactor.[147] Metal acetylacetonates were milled with flake graphite, which promoted bond cleavage and drove the species into the carbon interlayers. This confinement increased the local precursor concentration and promoted multimetal mixing. After mild 600 °C annealing, the authors obtained uniform PtFeCoNiMo HEA subnanoparticles of approximately 1.3 nm, which is consistent with confinement-limited growth. A more conventional route is direct milling of elemental powders. With respect to the V_x-CuCoNiFeMn system, Sivanantham *et al.* first mixed equimolar amounts of Cu, Co, Ni, Fe, and Mn and then added V to tune the composition.[52] High-energy planetary milling was performed under Ar using a process control agent and a high ball-to-powder ratio. The resulting powders were pressed into binder-free pellets as working electrodes.

4.5.3 Data-driven discovery and high-throughput synthesis. Data-driven discovery changes how HEA candidates are selected and tested.[18,148,149] Instead of manual trial-and-error, machine learning (ML) models prioritize a small set of compositions.[150,151] High-throughput synthesis and screening were then performed, and the samples were evaluated under uniform protocols. The new data are fed back into the model, and the next selection is refined. This closed loop reduces the time and cost while improving the search efficiency. It also addresses a core challenge in HEAs. The composition space is enormous, and classical exploration samples constitute only a small fraction.

High-throughput platforms accelerate the mapping of composition-performance relationships. These methods produce many samples in one run and measure them *via* consistent procedures. The resulting datasets are well suited for statistical learning and uncertainty-guided selection. In the best implementations, synthesis, screening, and modeling are tightly coupled. This yields faster iterations and more reliable structure–property inference. Shan *et al.* fabricated microscale HEA arrays by printing mixed salt precursors onto glassy carbon and converting them *via* rapid pulse heating, as shown in Fig. 11g.[125] Fast heating and quenching promoted mixing and reduced phase separation. They used the SECCM to screen intrinsic HER activity across many element combinations and compositions. The data were then coupled to an ensemble ML model that expanded the database and recommended candidates for validation. Pan *et al.* applied a related microscale strategy to the ORR.[48] They used a large language model (LLM) to mine the literature and define a focused element pool and then printed and pulse-heated quinary Pt-based HEA microdots. A key step was their intrinsic activity metric. Because embodied and scene-graph contextualized agent is difficult to quantify for each microdot, they used a relative current density definition to enable rapid ranking. Heatmap visualization then highlighted promising combinations, followed by validation and DFT interpretation of multimetal synergy. Kim *et al.* framed discovery as a multiobjective optimization problem and used Pareto active learning.[152] The model learned from the measured HER and OER overpotentials and proposed experiments that improved the Pareto front. They paired this with rapid synthesis by carbothermal shock and iterated until most of the space could be rejected with confidence.

Another strategy is to narrow the search before large experimental campaigns. An AI-assisted workflow first reduces the candidate pool *via* LLM-based literature mining.[153] A genetic algorithm then explores compositions through iterative selection and mutation. Thermal-shock-style synthesis accelerates experimental turnaround so that the loop can run quickly. The main benefit is that there are fewer experiments. The main risk is bias, since synthesis and evaluation constraints can steer the search. Zhou *et al.* demonstrated an inverse design framework that links robotics to a generative model built on spectroscopic descriptors.[154] The robotic platform produced high-throughput datasets *via* controlled procedures. The model learned

mappings from spectra to performance and from spectra to composition. It then generates candidate spectra that are predicted to perform well and translates them into compositions for validation. This is attractive for HEAs because spectra can encode local environments without explicit structural labels. Transferability remains a clear limitation. When chemical environments shift, learned correlations can fail, and models require retraining.

Across these five approaches, HEA synthesis is evolving from simple elemental mixing to controllable alloying and site engineering. Thermal routes remain robust and scalable, but often face sintering and limited surface control. Redox and electrochemical routes can offer better interfacial control, however, composition gradients and potential-driven reconstruction may blur structure assignment. Precursor-chemistry strategies can improve the uniformity and porosity, while external-energy inputs accelerate mixing but require careful calibration. Finally, data-driven and high-throughput workflows shorten iteration cycles, provided that descriptors and testing protocols are consistent and reproducible. Together, these advances motivate the following conclusions and outlook for the use of HEAs in the ORR and HER.

5. Conclusion and outlook

HEAs have been intensively explored as promising electrocatalysts. A wide range of compositional designs and synthetic routes have been investigated to clarify process–structure–property relationships. Their compositional complexity creates a broad distribution of local chemical environments and enables tunable electronic structures, allowing the adsorption energies of oxygenated and hydrogen intermediates to be optimized across different sites. In parallel, computational modeling is increasingly providing adsorption-energy databases and design guidance. Moreover, entropy-stabilized structures can help mitigate dissolution, segregation, and phase changes during electrochemical cycling. However, the same compositional complexity that enables tunability also complicates the identification of clear structure–function relationships, particularly under operating conditions where surfaces can dynamically evolve. In this review, we classified representative HEA catalysts in terms of their electronic structure and linked their composition to the d-band center, and we summarized common synthetic routes from a practical perspective. Despite rapid progress, several major challenges remain for HEAs in electrocatalysis, particularly for the ORR and HER. Key scientific opportunities and challenges include the following:

(1) Accelerated discovery and computational modeling: with the advent of ML tools, closed-loop workflows that combine first-principles calculations with reinforcement learning and high-throughput experimentation are becoming increasingly viable, enabling accelerated exploration of the vast composition space. However, the interpretability and transferability of data-driven models require further clarification, especially across electrolytes, potentials, and evolving surface states. Multi-objective constraints, *i.e.*, activity, stability, cost, and synthesizability, should also be defined more precisely to improve model robustness and practical relevance.

(2) Mechanistic understanding: multiple active sites in HEAs can be beneficial because distinct local chemical environments may favor different reaction steps. The role of entropy-related effects, potential-driven surface reconstruction/segregation, and the identity of the true active state should be explicitly analyzed, together with the rate-controlling steps under relevant conditions. Individual site contributions can be further resolved through combined modeling, *e.g.*, microkinetics, and advanced *in situ*/*operando* characterization.

(3) Morphological and structural control: transforming high-entropy mixing into controllable phase formation is essential. Synthetic strategies should target not only the average structure but also critical defects and near-surface composition. In particular, controlling the particle size (*e.g.*, nanoscale synthesis), surface/phase engineering, and support or confinement strategies will be key to maximizing the number of accessible active sites while maintaining long-term stability.

(4) Sustainability and practical deployment: compared with Pt or binary catalysts, HEAs include multi-objective composition design. It considers the simultaneous constraints of catalytic performance, cost and metal recovery. Substitution of scarce noble metals with earth-abundant components and design with circular economy principles are crucial. Recycling and recovery pathways for valuable metals in devices should be considered at the catalyst design stage. Ultimately, the most impactful catalysts and electrochemical devices will achieve net reductions in material demand and carbon emissions.

(5) Benchmarking and standardized evaluation: HEAs contain multielement surface ensembles and different active sites. This poses challenges for conventional benchmarking. These include different bulk and surface compositions, surface segregation or reconstruction during operation, and multielement dissolution or dealloying pathways. Phase characterization, electrochemical active surface area normalization details and quantitative analysis on nonnoble elements should be better addressed. Standardized posttest characterization is needed to correlate the performance with the surface composition and phase evolution.

(6) From half-cell performance to device relevance*:* Bringing the half-cell advantages of HEAs into membrane electrode assemblies is essential. On the one hand, the sluggish diffusion of HEAs mitigates dissolution. On the other hand, surface segregation, reconstruction, and redeposition become more complex because of the multiprincipal element design. Dissolution and redeposition in the catalyst layer, evolution of surface site ensembles in devices, and coupling of the ionomer distribution and porosity affect the practical current density. These factors could mask the intrinsic activity trends identified in half-cells. Testing under device-relevant conditions (including realistic catalyst loadings and durability protocols) will be critical to prioritize HEA compositions that truly translate.

(7) Dynamic surface evolution under operating conditions: HEAs may undergo potential-driven surface segregation, selective dissolution, oxidation, and reconstruction, leading to

catalytically active states that differ from those of the initial alloy. These changes can be electrolyte- and potential-window dependent, and may either increase activity, *e.g.*, *via* formation of active surface motifs, or accelerate degradation. *Operando* tracking of the near-surface composition/oxidation state, coupled with theory and kinetics, is essential for identifying stable active phases and design rules.

(8) Scalability, reproducibility, and impurity tolerance: controlling the homogeneity, phase purity, and surface composition at scale remains non-trivial, and batch-to-batch reproducibility is often underreported. Scalable synthesis routes should be paired with tight quality control, *i.e.*, composition, particle size distribution, and surface chemistry, and with performance validation across independent batches. Finally, the tolerance to impurities, *e.g.*, chloride, sulfur species, and organics, and electrolyte-specific degradation pathways should be evaluated under realistic feeds to better anticipate real-world operation.

Overall, translating HEAs from a versatile academic platform to practical ORR/HER catalysts will require convergent advances in operando-defined active states, predictive discovery, and device-relevant validation. If these challenges are addressed, HEAs could provide a scalable route to catalysts that simultaneously improve performance, durability, and material efficiency.

Conflicts of interest

The authors declare that they have no known competing financial interests or personal relationships that could have appeared to influence the work reported in this paper.

Data availability

No primary research results, software or code have been included and no new data were generated or analysed as part of this review.

Acknowledgements

We acknowledge support from the European Union Horizon 2020 research and innovation program under grant agreement no. 857470, and the European Regional Development Fund *via* the Foundation for Polish Science International Research Agenda PLUS program grant No. MAB PLUS/2018/8. S. B. acknowledges the National Science Centre, Poland for funding under the SONATA BIS programme (grant no. DEC-2023/50/E/ST3/00569). This work was carried out within the "Projektowanie Ulepszonych Szkieł Metalicznych" project (FENG.02.02-IP.05-0177/23) under the 2.2 First Team programme of the Foundation for Polish Science co-financed by the European Union from the European Funds for Smart Economy 2021–2027 (FENG). The publication was created within the framework of the project of the Minister of Science and Higher Education, Poland "Support for the activities of Centres of Excellence established in Poland under Horizon 2020" under contract no. MEiN/2023/DIR/3795.

References

1 L. Schlapbach and A. Züttel, *Nature*, 2001, **414**, 353–358.
2 Z. W. Seh, J. Kibsgaard, C. F. Dickens, I. Chorkendorff, J. K. Nørskov and T. F. Jaramillo, *Science*, 2017, **355**, eaad4998.
3 H. A. Gasteiger, S. S. Kocha, B. Sompalli and F. T. Wagner, *Appl. Catal., B*, 2005, **56**, 9–35.
4 J. K. Nørskov, T. Bligaard, A. Logadottir, J. R. Kitchin, J. G. Chen, S. Pandelov and U. Stimming, *J. Electrochem. Soc.*, 2005, **152**, J23.
5 R. He, S. Wang, L. Yang, S. Horta, Y. Ding, C. Di, X. Zhang, Y. Xu, M. Ibañez, Y. Zhou, S. Mebs, H. Dau, J. N. Hausmann, W. Huo, P. W. Menezes and A. Cabot, *Energy Environ. Sci.*, 2024, **17**, 7193–7208.
6 C. Wei, R. R. Rao, J. Peng, B. Huang, I. E. L. Stephens, M. Risch, Z. J. Xu and Y. Shao-Horn, *Adv. Mater.*, 2019, **31**, 1806296.
7 C. C. L. McCrory, S. Jung, I. M. Ferrer, S. M. Chatman, J. C. Peters and T. F. Jaramillo, *J. Am. Chem. Soc.*, 2015, **137**, 4347–4357.
8 M. Gong, Y. Li, H. Wang, Y. Liang, J. Z. Wu, J. Zhou, J. Wang, T. Regier, F. Wei and H. Dai, *J. Am. Chem. Soc.*, 2013, **135**, 8452–8455.
9 A. Lasia, *Int. J. Hydrogen Energy*, 2019, **44**, 19484–19518.
10 W. Sheng, H. A. Gasteiger and Y. Shao-Horn, *J. Electrochem. Soc.*, 2010, **157**, B1529–B1536.
11 J. K. Nørskov, J. Rossmeisl, A. Logadottir, L. Lindqvist, J. R. Kitchin, T. Bligaard and H. Jónsson, *J. Phys. Chem. B*, 2004, **108**, 17886–17892.
12 S. Li, L. Shi, Y. Guo, J. Wang, D. Liu and S. Zhao, *Chem. Sci.*, 2024, **15**, 11188–11228.
13 O. van der Heijden, S. Park, R. E. Vos, J. J. J. Eggebeen and M. T. M. Koper, *ACS Energy Lett.*, 2024, **9**, 1871–1879.
14 J. K. Nørskov, T. Bligaard, J. Rossmeisl and C. H. Christensen, *Nat. Chem.*, 2009, **1**, 37–46.
15 A. Kulkarni, S. Siahrostami, A. Patel and J. K. Nørskov, *Chem. Rev.*, 2018, **118**, 2302–2312.
16 W.-L. Hsu, C.-W. Tsai, A.-C. Yeh and J.-W. Yeh, *Nat. Rev. Chem.*, 2024, **8**, 471–485.
17 Y. Li, A. Olejarz, Ł. Kurpaska, E. Lu, M. J. Alava, H. S. Kim and W. Huo, *Int. J. Refract. Met. Hard Mater.*, 2024, **124**, 106834.
18 S. Wang, H. Yan, W. Huo, M. Abdellatief, F. Fang and P. H. C. Camargo, *ACS Appl. Mater. Interfaces*, 2025, **17**, 53587–53599.
19 D. B. Miracle and O. N. Senkov, *Acta Mater.*, 2017, **122**, 448–511.
20 W. Huo, S. Wang, F. J. Dominguez-Gutierrez, K. Ren, Ł. Kurpaska, F. Fang, S. Papanikolaou, H. S. Kim and J. Jiang, *Mater. Res. Lett.*, 2023, **11**, 713–732.
21 B.-S. Lou, Z.-T. Liu, C.-J. Wang, S. Wang, S.-H. Chen, N. Karuppusamy, C.-R. Hsing, W. Huo and J.-W. Lee, *J. Colloid Interface Sci.*, 2026, **702**, 138977.
22 N. J. van Eck and L. Waltman, *Scientometrics*, 2010, **84**, 523–538.

23 M. Nesselberger, S. Ashton, J. C. Meier, I. Katsounaros, K. J. J. Mayrhofer and M. Arenz, *J. Am. Chem. Soc.*, 2011, **133**, 17428–17433.
24 X. Jin, T. H. Gu, K. G. Lee, M. J. Kim, M. S. Islam and S. J. Hwang, *Coord. Chem. Rev.*, 2020, **415**, 213280.
25 G. Cao, S. Yang, J. C. Ren and W. Liu, *Nat. Commun.*, 2025, **16**, 1251.
26 Y. Qian, A. Tamm, D. Cereceda and S. Kang, *Comput. Mater. Sci.*, 2025, **252**, 113789.
27 Z. W. Chen, J. Li, P. Ou, J. E. Huang, Z. Wen, L. Chen, X. Yao, G. Cai, C. C. Yang, C. V. Singh and Q. Jiang, *Nat. Commun.*, 2024, **15**, 359.
28 Y. Li, C. K. Peng, Y. Sun, L. N. Sui, Y. C. Chang, S. Y. Chen, Y. Zhou, Y. G. Lin and J. M. Lee, *Nat. Commun.*, 2024, **15**, 10222.
29 J. K. Nørskov, F. Abild-Pedersen, F. Studt and T. Bligaard, *Proc. Natl. Acad. Sci. U. S. A.*, 2011, **108**, 937–943.
30 L. A. Kibler, A. M. El-Aziz, R. Hoyer and D. M. Kolb, *Angew. Chem., Int. Ed.*, 2005, **44**, 2080–2084.
31 S. Li, X. Tang, H. Jia, H. Li, G. Xie, X. Liu and H.-J. Qiu, *J. Catal.*, 2020, **383**, 164–171.
32 Z. Hu, K. Chen, Y. Zhu, B. Liu and J. Shen, *Small*, 2024, **20**, 2309819.
33 K. Tiwari, C. H. Wang, B. S. Lou, A. M. Demeku, I. Moirangthem, S. Wang, I. Rahmadtulloh, C. J. Wang, W. Huo and J. W. Lee, *J. Power Sources*, 2025, **654**, 237826.
34 S. Wang, H. Yan, W. Huo, A. Davydok, M. Zając, J. Stępień, H. Feng, Z. Xie, J. Shang, P. H. C. Camargo, J. Jiang and F. Fang, *Appl. Catal., B*, 2025, **363**, 124791.
35 W. A. Zoubi and N. Park, *Chem. Commun.*, 2025, **61**, 18590–18607.
36 W. Y. Huo, S. Q. Wang, W. H. Zhu, Z. L. Zhang, F. Fang, Z. H. Xie and J. Q. Jiang, *Tungsten*, 2021, **3**, 161–180.
37 Z. Li, Y. Duan, X. Liu, H. Pang, C. Dou, Y. Shi and W. Chen, *Adv. Funct. Mater.*, 2025, **35**, 2507152.
38 X. Yang, J. Feng, Y. Li, W. Zhu, Y. Pan, Y. Han, Z. Li, H. Xie, J. Wang, J. Ping and W. Tang, *Adv. Sci.*, 2024, **11**, 2406149.
39 P. Żeberek and B. Wiendlocha, *Mater. Today Commun.*, 2025, **47**, 113117.
40 S. Ming, K. Meng, C. Hou, L. Qin, S. Wang, J. Rong, X. Yu and H. Hou, *Phys. Chem. Chem. Phys.*, 2023, **25**, 32979–32988.
41 M. Shao, Q. Chang, J.-P. Dodelet and R. Chenitz, *Chem. Rev.*, 2016, **116**, 3594–3657.
42 S. Lee, J. Cho, J. H. Jang, J. Han, S. P. Yoon, S. W. Nam, T. H. Lim and H. C. Ham, *ACS Catal.*, 2016, **6**, 134–142.
43 R. Subbaraman, D. Tripkovic, D. Strmcnik, K.-C. Chang, M. Uchimura, A. P. Paulikas, V. Stamenkovic and N. M. Markovic, *Science*, 2011, **334**, 1256–1260.
44 R. He, L. Yang, Y. Zhang, X. Wang, S. Lee, T. Zhang, L. Li, Z. Liang, J. Chen, J. Li, A. O. Moghaddam, J. Llorca, M. Ibáñez, J. Arbiol, Y. Xu and A. Cabot, *Energy Storage Mater.*, 2023, **58**, 287–298.
45 K. Wang, R. Chen, H. Yang, Y. Chen, H. Jia, Y. He, S. Song and Y. Wang, *Adv. Funct. Mater.*, 2024, **34**, 2310683.
46 T. Chen, X. Zhang, H. Wang, C. Yuan, Y. Zuo, C. Gao, W. Xiao, Y. Yu, J. Cai, T. Luo, Y. Xiang and D. Xia, *Nat. Commun.*, 2025, **16**, 3308.
47 C. Madan, S. R. Jha, N. K. Katiyar, A. Singh, R. Mitra, C. S. Tiwary and A. Halder, *Energy Adv.*, 2023, **2**, 2055–2068.
48 Y. Pan, X. Shan, F. Cai, H. Gao, J. Xu and M. Zhou, *Angew. Chem., Int. Ed.*, 2024, **63**, e202407116.
49 K. Huang, X. Cao, Y. Lu, M. Xiu, K. Cui, B. Zhang, H. Zhang and Y. Huang, *Adv. Mater.*, 2024, **36**, 2304867.
50 C. Wang, J. Zhang, K. Miao, M. Long, S. Lai, S. Zhao and X. Kang, *Adv. Mater.*, 2024, **36**, 2400433.
51 Z. Chen, J. Wen, C. Wang and X. Kang, *Small*, 2022, **18**, 2204255.
52 A. Sivanantham, H. Lee, S. W. Hwang, H. U. Lee, S. B. Cho, B. Ahn and I. S. Cho, *Adv. Funct. Mater.*, 2023, **33**, 2301153.
53 A. Chandran M, P. Dutta, P. Singh, A. K. Singh and B. L. V. Prasad, *Adv. Funct. Mater.*, 2025, **35**, 2418644.
54 L. Su, H. Wu, S. Zhang, C. Cui, S. Zhou and H. Pang, *Adv. Mater.*, 2025, **37**, 2414628.
55 L. Tao, M. Sun, Y. Zhou, M. Luo, F. Lv, M. Li, Q. Zhang, L. Gu, B. Huang and S. Guo, *J. Am. Chem. Soc.*, 2022, **144**, 10582–10590.
56 T. A. A. Batchelor, J. K. Pedersen, S. H. Winther, I. E. Castelli, K. W. Jacobsen and J. Rossmeisl, *Joule*, 2019, **3**, 834–845.
57 T. A. A. Batchelor, T. Löffler, B. Xiao, O. A. Krysiak, V. Strotkötter, J. K. Pedersen, C. M. Clausen, A. Savan, W. Schuhmann, J. Rossmeisl and A. Ludwig, *Angew. Chem., Int. Ed.*, 2021, **60**, 6932–6937.
58 J. K. Pedersen, C. M. Clausen, O. A. Krysiak, B. Xiao, T. A. A. Batchelor, T. Löffler, V. A. Mints, L. Banko, M. Arenz, A. Savan, W. Schuhmann, A. Ludwig and J. Rossmeisl, *Angew. Chem., Int. Ed.*, 2021, **133**, 24346–24354.
59 W. Xu, E. Diesen, T. He, K. Reuter and J. T. Margraf, *J. Am. Chem. Soc.*, 2024, **146**, 7698–7707.
60 F. Sun, Q. Tang and D. Jiang, *ACS Catal.*, 2022, **12**, 8404–8433.
61 D. Wu, K. Kusada, T. Yamamoto, T. Toriyama, S. Matsumura, I. Gueye, O. Seo, J. Kim, S. Hiroi, O. Sakata, S. Kawaguchi, Y. Kubota and H. Kitagawa, *Chem. Sci.*, 2020, **11**, 12731–12736.
62 Y. Kang, O. Cretu, J. Kikkawa, K. Kimoto, H. Nara, A. S. Nugraha, H. Kawamoto, M. Eguchi, T. Liao, Z. Sun, T. Asahi and Y. Yamauchi, *Nat. Commun.*, 2023, **14**, 4182.
63 Y. Yu, Q. Wang, X. Li, Q. Xie, K. Xu, S. Zhang, H. Zhang, M. Gong and W. Lei, *Nano Mater. Sci.*, 2025, **7**, 400–408.
64 M. Wei, Y. Sun, J. Zhang, F. Ai, S. Xi and J. Wang, *Energy Environ. Sci.*, 2023, **16**, 4009–4019.
65 X. Fu, J. Zhang, S. Zhan, F. Xia, C. Wang, D. Ma, Q. Yue, J. Wu and Y. Kang, *ACS Catal.*, 2022, **12**, 11955–11959.
66 Y. Zou, L. Jing, J. Zhang, S. Luo, L. Wang, Y. Li, R. Goei, K. W. Tan and A. I. Y. Tok, *J. Mater. Chem. A*, 2024, **12**, 5668–5678.
67 X. Huang, Z. Wu, B. Zhang, G. Yang, H.-F. Wang, H. Wang, Y. Cao, F. Peng, S. Li and H. Yu, *Small*, 2024, **20**, 2311631.

68 X. Chen, C. Si, Y. Gao, J. Frenzel, J. Sun, G. Eggeler and Z. Zhang, *J. Power Sources*, 2015, **273**, 324–332.
69 R. K. Pittkowski, C. M. Clausen, Q. Chen, D. Stoian, W. van Beek, J. Bucher, R. L. Welten, N. Schlegel, J. K. Mathiesen, T. M. Nielsen, J. Du, A. W. Rosenkranz, E. D. Bøjesen, J. Rossmeisl, K. M. Ø. Jensen and M. Arenz, *EES Catal.*, 2023, **1**, 950–960.
70 Q. Mao, X. Mu, K. Deng, H. Yu, Z. Wang, Y. Xu, X. Li, L. Wang and H. Wang, *Adv. Funct. Mater.*, 2023, **33**, 2304963.
71 G. Feng, Y. Pan, D. Su and D. Xia, *Adv. Mater.*, 2024, **36**, 2309715.
72 H. Cai, H. Yang, S. He, D. Wan, Y. Kong, D. Li, X. Jiang, X. Zhang, Q. Hu and C. He, *Angew. Chem., Int. Ed.*, 2025, **64**, e202423765.
73 Y. Wang, W. Luo, S. Gong, L. Luo, Y. Li, Y. Zhao and Z. Li, *Adv. Mater.*, 2023, **35**, 2302499.
74 C. Chen, W. Wu, P. Chen, J. Guo, H. Bian, W. Li, X. Zhao and L. Wei, *Chem. Commun.*, 2025, **61**, 6787–6790.
75 Y. Tong, X. Li, X. Wang, L. Zhao, W. Luo, Z. Huang, P. Liu, Z. Yan, Y. Pan and W. Xing, *Adv. Mater.*, 2025, e17450.
76 Y. Wang, N. Gong, H. Liu, W. Ma, K. Hippalgaonkar, Z. Liu and Y. Huang, *Adv. Mater.*, 2023, **35**, 2302067.
77 C. Y. Ahn, J. E. Park, S. Kim, O. H. Kim, W. Hwang, M. Her, S. Y. Kang, S. Park, O. J. Kwon, H. S. Park, Y. H. Cho and Y. E. Sung, *Chem. Rev.*, 2021, **121**, 15075–15140.
78 J. Fan, M. Chen, Z. Zhao, Z. Zhang, S. Ye, S. Xu, H. Wang and H. Li, *Nat. Energy*, 2021, **6**, 475–486.
79 X. W. Lv, Z. Wang, Z. Lai, Y. Liu, T. Ma, J. Geng and Z. Y. Yuan, *Small*, 2024, **20**, 2306396.
80 L. Xia, P. Dai, C. Qu, Z. Yang, H. Zhen, K. Wang and M. Wu, *J. Mater. Chem. A*, 2025, **13**, 39382.
81 R. He, L. Yang, Y. Zhang, D. Jiang, S. Lee, S. Horta, Z. Liang, X. Lu, A. O. Moghaddam, J. Li, M. Ibáñez, Y. Xu, Y. Zhou and A. Cabot, *Adv. Mater.*, 2023, **35**, 2303719.
82 Y. Zhang, Q. Wan, L. Huang, T. Jiang, S. Wu, D. Li, Y. Liu, H. Wu and F. Ren, *J. Mater. Chem. A*, 2025, **13**, 17384–17392.
83 N. Schmitt, M. Schmidt, J. E. Mueller, L. Schmidt, M. Trabold, K. Jeschonek and B. J. M. Etzold, *Energy Adv.*, 2023, **2**, 854–863.
84 Z. Li, H. Zhong, X. Liu, F. K. Chiang, R. Li, H. Chen, X. Wang, C. Wan, Y. Wu, H. Wang, S. Jiang, X. Zhang and Z. Lu, *Adv. Mater.*, 2025, **37**, e202510703.
85 J. Xu, H. Sun, F. Cai, H. Liu, M. Hu, W. Liu, X. Shan, L. Yang, H. Gao, F. Zhao and M. Zhou, *Angew. Chem., Int. Ed.*, 2026, e202522707.
86 M. K. Plenge, J. K. Pedersen, L. A. Cipriano and J. Rossmeisl, *High Entropy Alloys & Mater.*, 2025, **3**, 165–177.
87 S. Wang, W. Huo, F. Fang, Z. Xie, J. K. Shang and J. Jiang, *Chem. Eng. J.*, 2022, **429**, 132410.
88 T. Priamushko, A. Kormányos and S. Cherevko, *Curr. Opin. Chem. Eng.*, 2024, **44**, 101020.
89 C. Luan, D. Escalera-Lopez, U. Hagemann, A. Kostka, G. Laplanche, D. Wu, S. Cherevko and T. Li, *ACS Catal.*, 2024, **14**, 12704–12716.
90 Y. Sun and S. Dai, *Sci. Adv.*, 2021, **7**, eabg1600.
91 Q. Ye, Y. Cheng and L. Cao, *ACS Catal.*, 2026, **16**, 2430–2442.
92 J. L. Bürgel, R. Zehl, F. Thelen, R. Zerdoumi, O. A. Krysiak, B. Kohnen, E. Suhr, W. Schuhmann and A. Ludwig, *Faraday Discuss.*, 2026, **264**, 64–82.
93 A. Li, N. Qureshi and V. Maheshwari, *Nanoscale*, 2025, **17**, 20020–20043.
94 S. L. A. Bueno, A. Leonardi, N. Kar, K. Chatterjee, X. Zhan, C. Chen, Z. Wang, M. Engel, V. Fung and S. E. Skrabalak, *ACS Nano*, 2022, **16**, 18873–18885.
95 M. W. Glasscott, *Curr. Opin. Electrochem.*, 2022, **34**, 100976.
96 P. Guo, D. Liu, Q. Wang, P. Chen, H. Yang, M. Zhang, C. Zheng, L. Jiang, H. Pan and R. Wu, *Nano Lett.*, 2025, **25**, 10209–10217.
97 J. K. Pedersen, T. A. A. Batchelor, D. Yan, L. E. J. Skjegstad and J. Rossmeisl, *Curr. Opin. Electrochem.*, 2021, **26**, 100651.
98 A. B. N. Alkraidi, M. Mansoor, B. Boztemur, H. Gökçe, F. Kaya, C. Yıldırım, B. Derin, D. Ağaoğulları and M. L. Öveçoğlu, *J. Alloys Compd.*, 2024, **1003**, 175510.
99 P. Kumari, A. Kumar, R. K. Mishra, M. A. Shaz, T. P. Yadav and R. R. Shahi, *J. Alloys Compd.*, 2023, **960**, 170697.
100 S. Duan, J. Kang, J. Cho, M. Lee, W. Mu and J. H. Park, *J. Alloys Compd.*, 2022, **928**, 167080.
101 X. Shen, G. Zhou, F. Liu, F. Dong, Y. Zhang, X. Yuan, B. Wang, L. Luo, Y. Su, J. Cheng and P. K. Liaw, *Intermetallics*, 2024, **173**, 108435.
102 Z. Huang, Y. Peng, L. Xing, M. Xu, M. Fang, H. Xie, J. Li, Y. Zhou, P. Wu, N. Wang, C. Tang, M. Wu, L. Wang, S. Ye and L. Du, *Appl. Catal., B*, 2025, **363**, 124775.
103 S. Gao, S. Hao, Z. Huang, Y. Yuan, S. Han, L. Lei, X. Zhang, R. Shahbazian-Yassar and J. Lu, *Nat. Commun.*, 2020, **11**, 2016.
104 S. Wang, B. Xu, W. Huo, H. Feng, X. Zhou, F. Fang, Z. Xie, J. K. Shang and J. Jiang, *Appl. Catal., B*, 2022, **313**, 121472.
105 H. Mahdavi, A. A. Alamdari, A. Kepceoğlu, M. B. Yağcı, U. Ünal and H. Jahangiri, *ACS Omega*, 2024, **9**, 22495–22505.
106 Y. Chida, T. Tomimori, T. Ebata, N. Taguchi, T. Ioroi, K. Hayashi, N. Todoroki and T. Wadayama, *Nat. Commun.*, 2023, **14**, 4492.
107 P. Wang, S. Guo, Y. Xu, X. Yuan, Y. Tian, B. Xu, Z. Zhao, Y. Wang, J. Li, X. Wang and Z. Liu, *ACS Nano*, 2025, **19**, 17589–17605.
108 J. Li, L. Zhou, Z. Zhang, C. Chen, X. Lv and J. Dang, *Adv. Funct. Mater.*, 2025, **36**, e17292.
109 Z.-L. Wang, G.-Y. Huang, G.-R. Zhu, H.-C. Hu, C. Li, X.-H. Guan and H.-B. Zhu, *Appl. Catal., B*, 2025, **361**, 124585.
110 H. Ye, J. Su, G. Yang, L. Zhou, Y. Xie, X. Zhan, J. Tian and X. Tong, *Mater. Today Commun.*, 2025, **45**, 112365.
111 A. Kumar, T. P. Yadav, M. A. Shaz and N. K. Mukhopadhyay, *Energy Storage*, 2024, **6**, e532.
112 A. V. Svalov, D. S. Neznakhin, A. V. Arkhipov, S. V. Andreev, A. S. Rusalina, A. V. Tebenkov, A. I. Medvedev, I. V. Beketov and G. V. Kurlyandskaya, *Appl. Phys. A*, 2025, **131**, 174.
113 Y. Ma, Z. Kou, W. Yang, A. He, Y. Dong, Q. Man, H. Liu, Z. Li, A. Inoue and J. Li, *Nat. Commun.*, 2024, **15**, 10549.

114 Z. Liu, E. Goudeli, R. Guo, H. Xie, Q. Luo, L. Zhao, W. Xu, J. J. Richardson, W. Xu, F. Caruso and S. Pan, *Nat. Chem.*, 2025, **17**, 1497–1504.
115 H. Schwarz, J. Apell, H. K. Wong, P. Henning, R. Wonneberger, N. Rösch, T. Uhlig, F. Ospald, G. Wagner, A. Undisz and T. Seyller, *Adv. Mater.*, 2023, **35**, 2301526.
116 S.-Y. Li, T.-X. Nguyen, Y.-H. Su, C.-C. Lin, Y.-J. Huang, Y.-H. Shen, C.-P. Liu, J.-J. Ruan, K.-S. Chang and J.-M. Ting, *Small*, 2022, **18**, 2106127.
117 T.-W. Lu, C.-S. Feng, Z. Wang, K.-W. Liao, Z.-Y. Liu, Y.-Z. Xie, J.-G. Hu and W.-B. Liao, *Appl. Surf. Sci.*, 2019, **494**, 72–79.
118 Y. Miyajima, H. Minowa, D. Tanada, P. P. Bhattacharjee, S. M. Lyth and K. Ishikawa, *Opt. Laser Technol.*, 2025, **191**, 113381.
119 Y. Yu, F. Xia, C. Wang, J. Wu, X. Fu, D. Ma, B. Lin, J. Wang, Q. Yue and Y. Kang, *Nano Res.*, 2022, **15**, 7868–7876.
120 Y. Li, C. Wang, K. Zhao, J. Ding, L. Deng, J. Gao and L. Xiao, *Catal. Sci. Technol.*, 2025, **15**, 4916–4921.
121 L. Yao, F. Zhang, S. Yang, H. Zhang, Y. Li, C. Yang, H. Yang and Q. Cheng, *Adv. Mater.*, 2024, **36**, 2314049.
122 H. Zhu, S. Sun, J. Hao, Z. Zhuang, S. Zhang, T. Wang, Q. Kang, S. Lu, X. Wang, F. Lai, T. Liu, G. Gao, M. Du and D. Wang, *Energy Environ. Sci.*, 2023, **16**, 619–628.
123 M. Xie, Y. Lu, X. Xiao, D. Wu, B. Shao, H. Nian, C. Wu, W. Wang, J. Gu, S. Han, M. Gu and Q. Xu, *Adv. Funct. Mater.*, 2025, **35**, 2414537.
124 D. Wu, L. Yao, M. Ricci, J. Li, R. Xie and Z. Peng, *Chem. Mater.*, 2022, **34**, 266–272.
125 X. Shan, Y. Pan, F. Cai, H. Gao, J. Xu, D. Liu, Q. Zhu, P.-P. Li, Z. Jin, J. Jiang and M. Zhou, *Nano Lett.*, 2024, **24**, 11632–11640.
126 X. Zhao, H. Cheng, X. Chen, Q. Zhang, C. Li, J. Xie, N. Marinkovic, L. Ma, J.-C. Zheng and K. Sasaki, *J. Am. Chem. Soc.*, 2024, **146**, 3010–3022.
127 Z. W. Chen, J. Li, P. Ou, J. E. Huang, Z. Wen, L. Chen, X. Yao, G. Cai, C. C. Yang, C. V. Singh and Q. Jiang, *Nat. Commun.*, 2024, **15**, 359.
128 M. Bollu, S. Prabhakaran, D. H. Kim, T. T. N. Ta, C.-L. Dong, T. A. Devi, D. T. Tran, N. H. Kim and J. H. Lee, *Appl. Catal., B*, 2026, **386**, 126399.
129 W. Huo, S. Wang, F. Fang, S. Tan, Ł. Kurpaska, Z. Xie, H. S. Kim and J. Jiang, *J. Mater. Res. Technol.*, 2022, **20**, 1677–1684.
130 L. Fu, H. N. Nam, J. Zhou, Y. Kang, K. Wang, Z. Zhou, Y. Zhao, L. Zhu, R. Nandan, M. Eguchi, Q. M. Phung, T. Yokoshima, K. Wu and Y. Yamauchi, *ACS Nano*, 2024, **18**, 27617–27629.
131 A. Aliyu and C. Srivastava, *Materialia*, 2019, **8**, 100459.
132 S. J. Percival, P. Lu, D. R. Lowry and T. M. Nenoff, *Langmuir*, 2022, **38**, 1923–1928.
133 S. Jo, M. C. Kim, K. B. Lee, H. Choi, L. Zhang and J. I. Sohn, *Adv. Energy Mater.*, 2023, **13**, 2301420.
134 W. Chen, C. Hu, J. Li, S. He, H. Liu and Z. Hua, *Langmuir*, 2025, **41**, 14345–14359.
135 T. Abid, M. A. Akram, T. B. Yaqub, M. R. A. Karim, F. Fernandes, M. F. Zafar and K. Yaqoob, *J. Alloys Compd.*, 2024, **970**, 172633.
136 L. Tao, M. Sun, Y. Zhou, M. Luo, F. Lv, M. Li, Q. Zhang, L. Gu, B. Huang and S. Guo, *J. Am. Chem. Soc.*, 2022, **144**, 10582–10590.
137 Z. Qiu, X. Guo, S. Cao, M. Du, Q. Wang, Y. Pi and H. Pang, *Angew. Chem., Int. Ed.*, 2025, **64**, e202415216.
138 J. Li, B. Li, P.-T. Li, N. Zhang and H.-S. Shang, *Rare Met.*, 2025, **44**, 1789–1799.
139 B. Niu, F. Zhang, H. Ping, N. Li, J. Zhou, L. Lei, J. Xie, J. Zhang, W. Wang and Z. Fu, *Sci. Rep.*, 2017, **7**, 3421.
140 Y. Li, Y. Y. Tay, P. J. S. Buenconsejo, W. Manalastas Jr., W. H. Tu, H. K. Lim, T. Salim, M. O. Thompson, S. Madhavi, C. Y. Tay and K. W. Tan, *Adv. Funct. Mater.*, 2023, **33**, 2211279.
141 Z. Liu, H. Li, C. Yang, M. Jiang, J. Zhang and C. Fu, *Small*, 2024, **20**, 2309078.
142 C. E. Park, J. Theerthagiri, V. Maheskumar, A. Kumar, G. H. Jeong and M. Y. Choi, *Small*, 2025, **21**, e2410304.
143 M. Liu, Z. Zhang, F. Okejiri, S. Yang, S. Zhou and S. Dai, *Adv. Mater. Interfaces*, 2019, **6**, 1900015.
144 K. M. B. Urs, N. K. Katiyar, R. Kumar, K. Biswas, A. K. Singh, C. S. Tiwary and V. Kamble, *Nanoscale*, 2020, **12**, 11830–11841.
145 H. Zhao, M. Liu, Q. Wang, Y. Li, Y. Chen, Y. Zhu, Z. Yue, J. Li, G. Wang, Z. Zou, Q. Cheng and H. Yang, *Energy Environ. Sci.*, 2024, **17**, 6594–6605.
146 R. B. Nair, H. S. Arora, P. Mandal, S. Das and H. S. Grewal, *Adv. Eng. Mater.*, 2018, **20**, 1800163.
147 S. Lu, Y. Hu, M. Hao, L. Xiong, D. Ma and Q. Yue, *Nano Res.*, 2025, **18**, 94907908.
148 Y. Li, H. Yan, S. Wang, X. Luo, Ł. Kurpaska, F. Fang, J. Jiang, H. S. Kim and W. Huo, *Mater. Des.*, 2025, **48**, 113497.
149 X. Luo, Y. Li, T. Mäkinen, S. Bonfanti, W. Huo and M. J. Alava, *Mater. Today Commun.*, 2025, **46**, 112464.
150 W. Zhu, W. Huo, S. Wang, X. Wang, K. Ren, S. Tan, F. Fang, Z. Xie and J. Jiang, *J. Mater. Res. Technol.*, 2022, **18**, 800–809.
151 W. Huo, *J. Mater. Sci.*, 2026, **61**, 2590–2603.
152 M. Kim, Y. Kim, M. Y. Ha, E. Shin, S. J. Kwak, M. Park, I.-D. Kim, W.-B. Jung, W. B. Lee, Y. Kim and H.-T. Jung, *Adv. Mater.*, 2023, **35**, 2211497.
153 Z. Fu, P. Huang, X. Wang, W.-D. Liu, L. Kong, K. Chen, J. Li and Y. Chen, *Adv. Energy Mater.*, 2025, **15**, 2500744.
154 D. Zhou, R. Yang, Z. Jia, Y. Cai, L. Zhao, L. Guo, G. Ye, S. Wang, L. Chen, D. Liu, P. E. S. Smith, Y. Huang, Q. Zhu and J. Jiang, *Nat. Synth.*, 2026, **5**, 119–128.

